# Induced polarization of clay-rich materials - Part 4: Water content and temperature effects in bentonites

J. El Alam, A. Revil, Pierre Dick

GEOPHYSICS, VOL. 90, NO. 2 (MARCH-APRIL 2025); P. MR39–MR54, 19 FIGS., 2 TABLES.
10.1190/GEO2024-0110.1





# Induced polarization of clay-rich materials — Part 4: Water content and temperature effects in bentonites

J. El Alam[1], A. Revil[2], and P. Dick[3]

## ABSTRACT

Deep geological disposals (DGDs) are widely seen to be the best solution to contain high-level radioactive wastes safely. Compacted bentonite and bentonite-sand mixtures are considered the most appropriate buffers or sealing materials for access drifts, ramps, and shafts due to their favorable physicochemical and hydromechanical properties. Bentonite-sand mixtures are expected to swell and seal all voids when in contact with water, forming an impermeable barrier to radioactive elements. The parameters that will most affect the hydraulic performance of these seals are their water content, dry density, water salinity, and temperature. Monitoring and assessing these parameters are, therefore, crucial to confirm that the seals' safety functions are fulfilled during the life of a DGD. Induced polarization (IP) is a nonintrusive geophysical method able to perform this task. However, the underlying physics of bentonite-sand mixtures has not been checked. The complex conductivity spectra of 42 compacted bentonite-sand mixtures are measured in the frequency range of 1 Hz–45 kHz in order to develop workable relationships between in-phase and quadrature conductivities versus water content and saturation, pore water conductivity, bentonite-sand ratio (10% to 100%), temperature (10°C–60°C), and dry density (0.97 to 1.64 g cm$^{-3}$). We observe that conductivity is mostly dominated by surface conductivity associated with the Stern layer coating the surface of smectite, the main component of bentonite. At a given salinity and temperature, the in-phase and quadrature conductivities obey power law relationships with water content and saturation. The in-phase and quadrature conductivities depend on temperature according to a classical linear relationship with the same temperature coefficient. A Stern layer-based model is used to explain the dependence of the complex conductivity with water content, dry density, water salinity, and temperature. It could be used to interpret IP field data to monitor the efficiency of the seal of DGD facilities.

## INTRODUCTION

Countries with commercial nuclear power production are planning to isolate their high-level and long-lived radioactive waste in deep geological disposal (DGD) to avoid any discharge of radionuclides in the biosphere (Madsen, 1998; McCombie et al., 2000; Mckinley et al., 2007; Palmu and Torsten, 2010). DGDs involve isolating radioactive waste within a stable geologic environment (typically at a depth of 400–600 m). This is generally achievable by using multiple barriers acting together to provide protection over hundreds of thousands of years (Ewing et al., 2016). These multiple barrier systems include a host rock (such as the Callovo-Oxfordian (COx) formation in France, the Opalinus clay in Switzerland, or the migmatitic gneiss and pegmatitic granite in Olkiluoto, Finland) and an engineered barrier system (EBS). The EBS is composed of a waste form, waste canisters, buffer materials, backfills, seals, and concrete plugs (see OECD, 2003; Mckinley et al., 2007; Sellin and Leupin, 2013, Figure 1).

Manuscript received by the Editor 17 February 2024; revised manuscript received 21 August 2024; published ahead of production 1 November 2024; published online 7 January 2025.
[1]Université Grenoble Alpes, Université Savoie Mont Blanc, CNRS, EDYTEM, Le Bourget du Lac, France and Institut de Radioprotection et de Sûreté Nucléaire (IRSN), PSE-ENV/SPDR/LETIS, Fontenay-aux-Roses, France. E-mail: jad.elalam@irsn.fr.
[2]Université Grenoble Alpes, Université Savoie Mont Blanc, CNRS, EDYTEM, Le Bourget du Lac, France. E-mail: andre.revil@univ-smb.fr (corresponding author).
[3]Institut de Radioprotection et de Sûreté Nucléaire (IRSN), PSE-ENV/SPDR/LETIS, Fontenay-aux-Roses, France. E-mail: pierre.dick@irsn.fr.

DOI:10.1190/geo2024-0110.1

In the French geological disposal project (called CIGEO), the sealing of the galleries, access ramps, and shafts to prevent potential pathways for water, gas, and radionuclides migration is one of the key points to ensure the long-term safety of the repository (Mokni et al., 2016; Mokni and Barnichon, 2016). Bentonite is generally regarded as the most suitable sealing material (Delage et al., 2010; Tournassat et al., 2015). This is due to its high swelling ability, low permeability, thermal stability, and high retention properties with a large surface area and cation exchange capacity (CEC) (Kanno and Wakamatsu, 1992; Chapman, 2006; Villar and Lloret, 2008; Chen et al., 2014). For applications in geologic disposals, the bentonite is usually installed as compacted blocks of bentonite-sand mixtures or pure bentonite pellets (Cui et al., 2008; Villar et al., 2008; Gens et al., 2009; Ye et al., 2010; Wang et al., 2013; Saba, 2013; Wang et al., 2015). In repository conditions, the compacted sand-bentonite mixtures will be set up in unsaturated conditions. The water content of bentonite is expected to increase through the suction and sorption of groundwater from the surrounding formation. This infiltration would, in turn, trigger the development of swelling pressures (Villar and Lloret, 2008; Dieudonné et al., 2016; Mokni and Barnichon, 2016). One of the major roles of swelling is to ensure that the sealing material closes all the macro-voids in the disposal. It is well documented that swelling pressure and permeability depend principally on the saturation and dry density of the material (e.g., Imbert and Villar, 2006). A small change in density can induce a significant change in swelling pressure and permeability. Such behavior may, in turn, influence the hydromechanical behavior of the sand-bentonite mixture (Villar and Lloret, 2008; Shirazi et al., 2010; Darde et al., 2022).

The addition of sand to bentonite improves certain characteristics, such as increasing the dry density and shear strength and decreasing the shrinkage (Dixon et al., 1985; Srikanth and Mishra, 2016). It presents hydraulic conductivities similar to pure bentonite

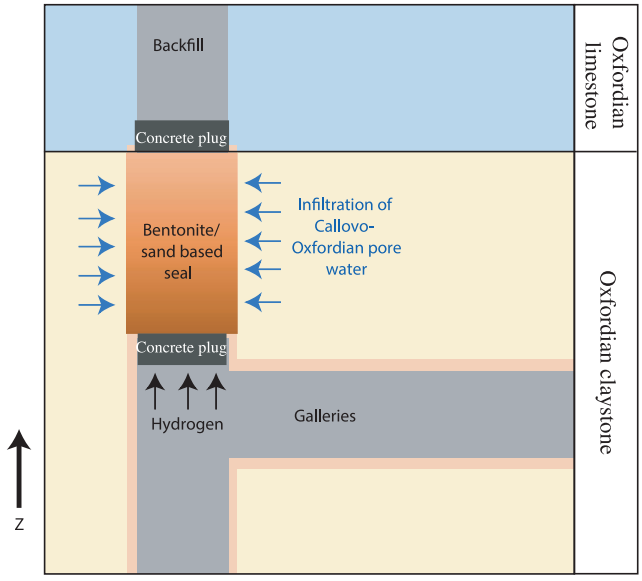


Figure 1. Sketch of the vertical shaft in CIGEO highlighting the migration pathway for hydrogen ($H_2$) gas. The migrating gas causes a pressure buildup at the lower interface between the concrete core and the sealing core made of a mixture of bentonite and sand. The addition of sand may improve the gas permeability of the core.

(Cho et al., 2000). Increasing the sand content within the seal favors gas-pathways within the repository (Smart et al., 2008; Bardelli et al., 2014; Guo et al., 2020). This may help avoid the accumulation of gas (particularly hydrogen) that is expected to be produced by the radiolysis of water due to ionizing radiation and the anaerobic corrosion of steel and reactive metals present in the disposal facility (Guo et al., 2020). The effect of hyperalkaline solution (associated with the presence of cement) is discussed in the next paper of this series (El Alam et al., 2024).

Monitoring parameters such as water content, dry density, saturation, salinity, and permeability through space in a sand-bentonite seal can, therefore, be considered essential to assess and monitor the long-term performance of these seals. The effect of temperature is also of paramount importance in interpreting the in situ experiments in field conditions. Different monitoring technologies sensitive to such a broad range of parameters have been tested to assess their efficiency for DGDs (e.g., Bertrand et al., 2019). The sensors include total pressure cells, pore pressure sensors, thermocouples, time-domain and frequency-domain reflectometry sensors, and fiber optics (see details in Müller et al., 2015; García-Siñeriz et al., 2019; Sakaki et al., 2019). These technologies tend to give accurate readings. That said, they provide only local information, and their setting may offer a preferential pathway for the migration of radionuclides.

In contrast, geophysical methods provide powerful alternatives (or complementary techniques) because (1) they can be designed in a nonintrusive manner, (2) they are sensitive to variations in water and clay content, (3) they allow dynamic phenomena to be monitored over time, and (4) they allow local anomalies to be captured that are potentially missed by localized sensors. A broad range of geophysical methods such as seismic tomography and electrical resistivity tomography (ERT) have already been tested for operational repository monitoring (Biryukov et al., 2016; Wieczorek et al., 2017; De Carvalho Faria Lima Lopes et al., 2019; Maurer et al., 2019; Ducut et al., 2022; Wayal and Sitharam, 2022). However, seismic monitoring experiments have shown that entirely nonintrusive traveltime tomography could be challenging as it can have difficulties in detecting subtle changes within a low-velocity and attenuating environment (Manukyan et al., 2012).

Induced polarization (IP) can be conducted in parallel with ERT surveys. This method yields additional information by exploring the low-frequency polarization mechanisms that occur when an electrical field is applied, either in time or frequency domains (Wait, 1959; Telford et al., 1990; Ward, 1990). Pioneered a century ago by Schlumberger (1920), IP has been applied since to multiple fields and topics, such as the study of the excavation damaged zones (Kruschwitz and Yaramanci, 2004; Okay et al., 2013), ore exploration (Martin et al., 2022), salinity variations in nonconsolidated clays and sandstones (Weller et al., 2011; Mendieta Tenorio, 2021), biogeophysics (Atekwana and Slater, 2009; Martin and Günther, 2013; Mendonça et al., 2015; Song et al., 2022), the study of the critical zone of the earth (Weller et al., 2011, 2013; Jougnot, 2020), the alteration of volcanic rocks (Revil et al., 2021), permafrost (Duvillard et al., 2018; Mudler et al., 2019, 2022), and geoarcheology (Martin et al., 2020).

In IP, conduction and polarization by a primary electrical field are studied in the low-frequency limit (<10 kHz) of the Maxwell equations (Vinegar and Waxman, 1984). The IP of low-porosity, anisotropic clay rocks and illite/pyrites mixes is investigated in the three

DOI:10.1190/geo2024-0110.1

previous papers of this series (Revil et al., 2023a, 2023b, 2024). However, the IP properties of high CEC, high porosity, and smectite-rich materials need to be investigated as an end-member case of clay-rich materials.

Many works have been published to elucidate the polarization of clay-rich media (e.g., Cosenza et al., 2007; Leroy and Revil, 2009; Jougnot et al., 2010; Breede et al., 2012; Revil et al., 2013, 2017, 2018b; Okay et al. 2013, 2014). In the past, various models have been developed to advance the petrophysics of the IP of clay-rich materials, including the double-layer polarization model of De Lima and Sharma (1992) and Lyklema et al. (1983), the generalized effective-medium theory of IP (GEMTIP) model based on the differential effective medium theory (Zhdanov, 2008; Tong et al., 2023), and the diffuse layer polarization models initially developed for colloidal suspension (e.g., Dukhin and Shilov, 1974; Fixman, 1980; Barreto and Dias, 2014). Other models are based on different physics, such as the membrane polarization model (Marshall and Madden, 1959; Li et al., 2021). The model of Cosenza et al. (2008) is based on the Maxwell-Wagner polarization but cannot explain the low-frequency IP features, such as the relationship between surface conductivity and normalized chargeability. Actually, none of these fundamental models can explain large data sets of experimental data. Indeed, in porous media, at the opposite of dilute colloidal suspensions of clays, the diffuse layers overlap and therefore cannot be easily polarized. As a consequence, early emphasis has been put on the so-called dynamic Stern layer model (see Stern [1924] for the original description; see Rosen and Saville [1991] and Grosse [2009] for a dynamic Stern layer model applied to IP). The GEMTIP model is not based on any physical polarization mechanisms and should be coupled to such mechanisms to be predictive (see the discussion in Revil and Cosenza, 2010). The membrane polarization model is unable to explain experimental data, possibly indicating that membrane polarization may not be the dominant polarization mechanism at play in the conditions used to measure IP phenomena.

Conversely, semiempirical models have been developed by Waxman and Smits (1968) for conduction and Vinegar and Waxman (1984) for polarization of clay-bearing sediments. The model of Vinegar and Waxman (1984) is compatible with a dynamic Stern layer model coupled to a membrane mechanism. The dynamic Stern layer polarization model developed by Revil (2013a, 2013b) is based on volume-averaging upscaling and offers a physics-based model that is entirely compatible with the models of Waxman and Smits (1968) and Vinegar and Waxman (1984). This model, very simple in essence, is therefore used in this paper as a starting basis to explain and elucidate the IP properties of bentonite-sand mixtures.

In this paper, we conducted IP measurements on 42 manufactured samples composed of mixtures of Fontainebleau sand (pure silica, poorly polarizable) and MX80 Wyoming bentonite (highly polarizable). The choice of the frequency range was performed for four reasons: (1) frequencies below 1 Hz were not considered in order to speed up the experimental work (a lot of spectra needed to be done in a reasonable amount of time); (2) smectite particles polarize at high frequencies (>10 Hz); (3) time-domain IP is usually performed at 1 Hz in field conditions, which is inside the frequency range investigated here; and (4) electrode drift can complicate the accuracy of the measurements below 1 Hz.

Our first goal of this study is (1) to establish a database for the complex conductivity spectra of bentonite-sand mixtures at different mass fractions of bentonite and volumetric water contents. In terms of petrophysical parameters, the range of volumetric water contents is 19% to 76%, saturation is 40% to 100%, dry density is 0.98 to 1.61, and the mass fractions of clay are 10% to 90% (100% if we consider the data from El Alam et al., 2023). These conditions are those that may be encountered in the early and late times of the life of a DGD (Gens et al., 2009; Ye et al., 2010; Saba, 2013). (2) Our second goal is to explain the observed trends found between the complex conductivity spectra and mass fraction of bentonite at different saturation states and bentonite contents. (3) We also test a simple linear temperature dependence equation for in-phase and quadrature conductivities and normalized chargeability.

## MATERIALS AND METHODS

### Measurements performed at 25°C

The data set studied in this paper is composed of a total of 42 experiments/samples (see Table 1). The entire data set is made up of mixtures of Wyoming MX80 bentonite, which is composed of crushed pellets at a relatively homogeneous granulometry (Molinero Guerra et al., 2017), and Fontainebleau sand (Figure 2). The MX80 bentonite is mostly composed of Montmorillonite (70% to 90% dry weight) plus quartz, feldspar, muscovite, and calcite. The Fontainebleau sand is a quartz sand (99.98% silica) with a narrow grain size distribution and a mean grain diameter of approximately 250 μm (Bourbié and Zinszner, 1985; Doyen, 1988). The Fontainebleau sand is characterized by a very weak polarization compared with the polarization of bentonite (compare the results of Revil et al. [2014a] for the Fontainebleau sandstone and those of El Alam et al. [2023] for pure bentonite).

The procedure for the creation of the bentonite-sand samples starts by spraying deionized water and crushed pellets of powder on the sand and mixing the three components together (Figure 2). The spraying is done until the desired water content is reached. The hydrated bentonite-sand mixture is then placed in a metallic mold and compacted to a given density using a uniaxial press with uniaxial confining pressure (see Bairlein et al., 2014). Such sample preparation leads to samples that are homogeneous, at least through visual inspection (Figure 2). The compaction states (height, bulk density, dry density, and porosity), as well as the saturations and initial water content, were measured and/or calculated after compaction. The samples have a diameter of 5 cm and heights ranging between 6 and 8 cm (see Figure 2).

Electrocardiogram (ECG) electrodes (pregelled Ag-AgCl) are then placed on the samples, and complex conductivity spectra are obtained using the high-precision impedance meter and a four electrode array, separating the voltage electrodes from the current electrodes (Figure 2). The measurements were done within 10 min after a sample was compacted to minimize its dehydration through drying. The electrodes were placed in a radial configuration, implying four electrodes being placed at 90° from each other and at the center height of each sample (see Jougnot et al., 2010; Okay et al., 2014; and Figure 2). Two current electrodes (A and B) impose the current, and then two potential electrodes (M and N) measure the potential difference.

Transforming the measured impedance (in Ω) into complex conductivity (in $S\,m^{-1}$) requires a geometric factor $K$ (in meters). We numerically determined $K$ using COMSOL Multiphysics to be 0.23 and 0.25 m for sample heights of 6 and 8 cm (depending on the

**Table 1. Results of the 42 experiments.**

| ID | $\theta$ (-) | $s_w$ (-) | $\rho_b$ (g cm$^{-3}$) | $\rho_b$ (g cm$^{-3}$) | $\phi$ (-) | $\sigma'$ (345 Hz) (S m$^{-1}$) | $\sigma''$ (345 Hz) (S m$^{-1}$) | $M_n$ (S m$^{-1}$) | Mass (%) |
|---|---|---|---|---|---|---|---|---|---|
| E70 | 0.42 | 0.87 | 1.82 | 1.39 | 0.48 | 0.112843 | 0.000855 | 0.002388 | 0.5 |
| E71 | 0.43 | 0.90 | 1.83 | 1.4 | 0.48 | 0.090738 | 0.000971 | 0.003993 | 0.3 |
| E72 | 0.39 | 0.74 | 1.69 | 1.28 | 0.53 | 0.15134 | 0.000689 | — | 0.7 |
| E73 | 0.55 | 1.00 | 1.85 | 1.22 | 0.55 | 0.311832 | 0.002919 | 0.014275 | 0.7 |
| E74 | 0.64 | 1.00 | 1.69 | 0.98 | 0.64 | 0.329625 | 0.003945 | 0.01773 | 0.7 |
| E75 | 0.54 | 1.00 | 1.88 | 1.24 | 0.54 | 0.275068 | 0.003018 | 0.011622 | 0.5 |
| E76 | 0.60 | 1.00 | 1.83 | 1.07 | 0.60 | 0.251981 | 0.003205 | 0.014179 | 0.5 |
| E77 | 0.53 | 1.00 | 1.9 | 1.26 | 0.53 | 0.176399 | 0.002348 | 0.006791 | 0.3 |
| E78 | 0.38 | 0.67 | 1.61 | 1.22 | 0.56 | 0.151403 | 0.000637 | 0.002296 | 0.9 |
| E79 | 0.57 | 0.97 | 1.72 | 1.13 | 0.59 | 0.358968 | 0.002897 | 0.011981 | 0.9 |
| E80 | 0.41 | 1.00 | 1.67 | 0.97 | 0.65 | 0.408275 | 0.004208 | 0.016463 | 0.9 |
| E81 | 0.17 | 0.41 | 1.83 | 1.64 | 0.41 | 0.013566 | 0.000094 | 0.000373 | 0.9 |
| E82 | 0.40 | 0.81 | 1.73 | 1.33 | 0.50 | 0.034169 | 0.000643 | — | 0.1 |
| E84 | 0.29 | 0.60 | 1.71 | 1.41 | 0.48 | 0.066113 | 0.000343 | — | 0.5 |
| E85 | 0.27 | 0.53 | 1.62 | 1.34 | 0.51 | 0.077555 | 0.000262 | — | 0.7 |
| E86 | 0.30 | 0.67 | 1.84 | 1.51 | 0.45 | 0.137856 | 0.000345 | — | 0.9 |
| E87 | 0.50 | 1.00 | 1.91 | 1.36 | 0.50 | 0.267206 | 0.002805 | 0.016914 | 0.5 |
| E88 | 0.49 | 1.00 | 1.92 | 1.37 | 0.49 | 0.243691 | 0.003591 | 0.020678 | 0.3 |
| E89 | 0.52 | 1.00 | 1.85 | 1.31 | 0.52 | 0.283429 | 0.00247 | 0.0091 | 0.7 |
| E90 | 0.53 | 1.00 | 1.85 | 1.3 | 0.53 | 0.30615 | 0.001823 | 0.003428 | 0.9 |
| E91 | 0.61 | 1.00 | 1.75 | 1.08 | 0.61 | 0.337988 | 0.003384 | 0.015791 | 0.9 |
| E149 | 0.57 | 1.00 | 1.72 | 1.15 | 0.57 | 0.302879 | 0.004489 | 0.018567 | 0.5 |
| E150 | 0.27 | 0.54 | 1.76 | 1.17 | 0.50 | 0.384864 | 0.004830 | 0.000578 | 0.5 |
| E151 | 0.31 | 0.59 | 1.79 | 1.19 | 0.53 | 1.312728 | 0.007009 | 0.000749 | 0.5 |
| E152 | 0.26 | 0.50 | 2.00 | 1.58 | 0.52 | 0.703999 | 0.000842 | 0.000119 | 0.5 |
| E153 | 0.21 | 0.48 | 1.74 | 1.53 | 0.44 | 0.018656 | 4.22E-05 | — | 0.5 |
| E154 | 0.19 | 0.44 | 1.70 | 1.51 | 0.44 | 0.014214 | 0.000387 | — | 0.3 |
| E155 | 0.24 | 0.55 | 1.75 | 1.51 | 0.44 | 0.008168 | 5.62E-05 | 0.00017 | 0.3 |
| E156 | 0.16 | 0.40 | 1.77 | 1.61 | 0.40 | 0.006647 | — | — | 0.3 |
| E157 | 0.25 | 0.58 | 1.79 | 1.54 | 0.43 | 0.041427 | 0.0002148 | 0.000764 | 0.4 |
| E158 | 0.24 | 0.55 | 1.74 | 1.50 | 0.44 | 0.027041 | 0.0001369 | 0.000372 | 0.4 |
| E159 | 0.33 | 0.76 | 1.86 | 1.53 | 0.43 | 0.08557 | 0.0006114 | 0.002303 | 0.4 |
| E161 | 0.23 | 0.51 | 1.71 | 1.47 | 0.46 | 0.019042 | 8.96E-05 | 0.000267 | 0.4 |
| E162 | 0.37 | 0.82 | 1.86 | 1.49 | 0.45 | 0.09231 | 0.0007204 | 0.002831 | 0.4 |
| E163 | 0.41 | 0.92 | 1.90 | 1.50 | 0.45 | 0.110976 | 0.001002 | 0.004311 | 0.4 |
| E164 | 0.28 | 0.61 | 1.76 | 1.48 | 0.46 | 0.056842 | 0.000200 | — | 0.6 |
| E165 | 0.38 | 0.83 | 1.87 | 1.50 | 0.45 | 0.151854 | 0.000844 | — | 0.6 |
| E166 | 0.29 | 0.64 | 1.80 | 1.52 | 0.45 | 0.080557 | 0.000254 | 0.000913 | 0.6 |
| E167 | 0.22 | 0.47 | 1.67 | 1.45 | 0.47 | 0.032405 | 9.39E-05 | 0.000168 | 0.6 |
| E168 | 0.25 | 0.54 | 1.72 | 1.47 | 0.46 | 0.037069 | 8.73E-05 | 0.000152 | 0.6 |
| E169 | 0.42 | 0.90 | 1.89 | 1.48 | 0.46 | 0.161469 | 0.000985 | 0.003778 | 0.6 |
| E170 | 0.46 | 1.00 | 1.94 | 1.48 | 0.45 | 0.196955 | 0.001361 | 0.00545 | 0.6 |

Note: "ID" describes the experiment number and, therefore, the sample identity. Here, $\Theta$ denotes the water content. The quantities $\rho_b$ and $\rho_d$ denote the bulk density (at a given water content) and the dry density, respectively. The quantity $\phi$ denotes the connected porosity. The parameter $s_W$ denotes the (water) saturation ($s_W$ = 1 for full saturation). The quantity $\gamma_b$ denotes the mass fraction of bentonite. Finally, the quantities $\sigma'$ and $\sigma''$ denote the in-phase conductivity determined at a frequency of 345 Hz, respectively, and $M_n$ denotes the normalized chargeability taken as the difference of the in-phase conductivity between 10 Hz and 10 kHz. The water content is obtained using $\theta = m_w/(\rho_w V)$, where $m_w$ (in kg) is the total mass of water (in kg) present in the samples (measured), $V$ (in m$^3$) denotes the total volume of the sample (measured), and $\rho_w$ is the mass density of water (approximately 1000 kg m$^{-3}$ in the following, known). We calculate the bulk and dry densities of the samples according to $\rho_b = (m_w + m_s)/V$ and $\rho_d = \rho_b/(1 + w)$, and $w$ is the weight fraction of water (we use 2770 and 2650 kg m$^{-3}$ for the grain densities of bentonite and Fontainebleau sand, respectively). The connected porosity $\phi = V_p/V$ (dimensionless) and water saturation $s_w = V_w/V_p$ (dimensionless) are also reported in the table ($V_p$ and $V_w$ denote the volumes of pore and water, respectively). The measurements were done at 23°C ± 2°C.

degree of compaction), respectively. The procedure to obtain the geometric coefficient is discussed in Jougnot et al. (2010) and is based on numerically solving Ohm's law with the charge conservation equation, adding the appropriate boundary conditions for the potential and current.

The complex conductivity spectra are obtained using a high-precision MFIA impedance analyzer manufactured by Zurich Instruments (Figure 2a). The total number of measuring points per sweep was set to 100, regardless of the frequency range. Replicates indicate that the in-phase conductivity has an accuracy of 2%, whereas the quadrature conductivity has an accuracy of 5% in the frequency range investigated in this study (1 Hz–45 kHz). Examples of complex conductivity spectra are shown in Figure 3 for different bentonite and water contents and in Figure 4 at different temperatures.

When using deionized water, the true pore water conductivity remains unknown because of the interaction between water and the hydrated ions in the micro- and nanoporosity of the bentonite and possibly salt crystals. Samples E70 to E91 and E153 to E170 were hydrated with deionized water, whereas samples E149 to E152 were saturated with saline solutions (NaCl) of known conductivities. The saline solutions used for samples E149 to E152 correspond to the following four saline solution conductivities $\sigma_w$ (NaCl, 25°C) = 0.2, 1.0, 5.0, and 10 S m$^{-1}$ (or approximately 1.3, 6.5, 32.5, and 65 g/L), respectively. These conductivities were checked through measurements. Samples E149 to E151 all had porosities of approximately 0.58 ± 0.01, whereas E152 had a lower porosity of 0.41. These experiments were performed in order to estimate the pore water conductivity when the samples were mixed with the deionized water after one hour of equilibrium time.

Figure 5 shows the conductivity data for eight fully saturated samples at porosities of approximately 0.57 ± 0.02. These conductivity data confirm a high degree of linearity between the conductivity of bentonite, bentonite-sand mixtures, and the pore water conductivity. All the conductivity data were fitted with the best fit of the classical linear conductivity equation $\sigma_\infty = \sigma_w/F + \sigma_S$ (Waxman and Smits, 1968) to determine the formation factor $F$ and the surface conductivity $\sigma_S$ assuming that the salinity dependence of the surface conductivity can be neglected. The salinity and pore water composition dependence of surface conductivity are discussed in Vaudelet et al. (2011a, 2011b) and Weller et al. (2011, 2013) whereas they are neglected in this study (e.g., Revil, 2012).

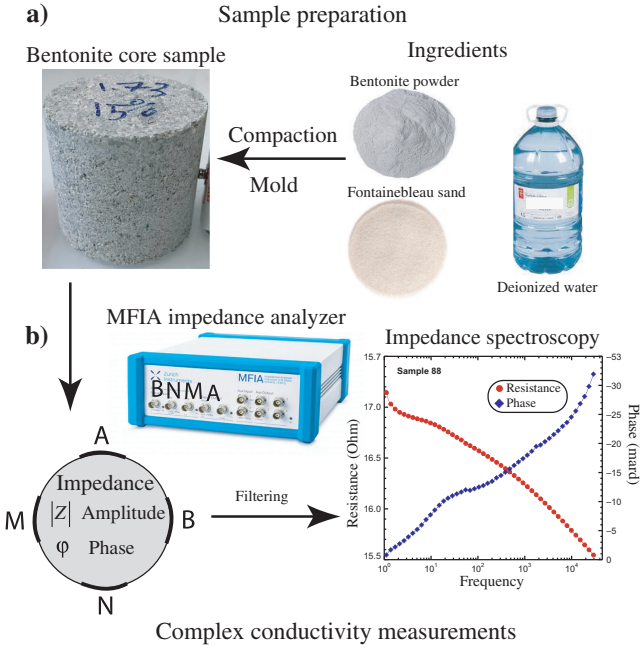


Figure 2. Sample preparation and impedance spectroscopy. (a) Sample preparation by using three ingredients (bentonite powder, Fontainebleau sand, and deionized water) and mixing them before compacting the mixture in a mold and using a press to obtain a cylindrical sample at the desired clay and water contents. (b) Electrical impedance spectroscopy. Position of the electrodes (A and B are the current electrodes, and M and N are the voltage electrodes). The measurements are made with a Zurich Instruments MFIA Impedance Analyzer used to measure the impedance spectrum in the frequency range 1 mHz–45 kHz.

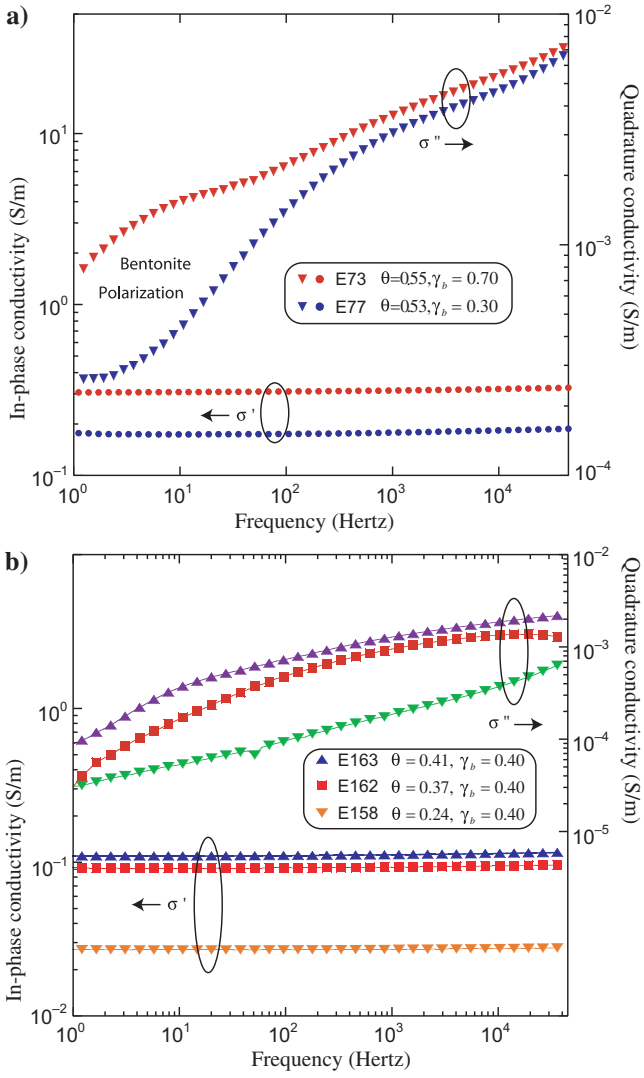


Figure 3. Examples of in-phase and quadrature conductivity spectra of fabricated samples at different saturations and bentonite contents (see the properties in Table 1). The data are recorded in the frequency range of 1 Hz to 45 kHz. Here, $\gamma_B$ denotes the bentonite content as a weight fraction, whereas θ denotes the volumetric water content. (a) Two samples with nearly the same water content and distinct clay contents and (b) three samples with the same clay content and different water contents.

The volumetric water contents, porosity, and saturation of the 42 experiments are reported in Table 1. We assume no unconnected porosity is present in these granular materials. The CEC of the MX80 used in this study was determined using the cobaltihexamine method (Guillaume, 2002; Bradbury and Baeyens, 2003; Molinero Guerra et al., 2017). We obtained a value of 87.2 ± 0.64 cmol(+)/kg (81.9 meq/100 g) for three replicates. We also measured the hygroscopic water content of MX80 after drying the samples at 105°C for 120 h.

We now use the curve of the (in-phase) conductivity versus the pore water conductivity using four experiments (fully saturated, samples E149 to E152, Table 1) discussed previously to determine the pore water conductivity in the other experiments. We measured the in-phase conductivity of a sample prepared under the same conditions but with deionized water (sample E75, $\phi = 0.54$, fully saturated, see Table 1). The conductivity of the pore water is obtained by using the projection of the in-phase conductivity and the curve to obtain the pore water conductivity (see Figure 2). We find a pore water conductivity of 0.28 S m$^{-1}$ at 25°C. Because we always use the same bentonite powder, the pore water conductivity is assumed to remain the same at a given temperature for all the experiments in Table 1, with the exception of E149 to E152.

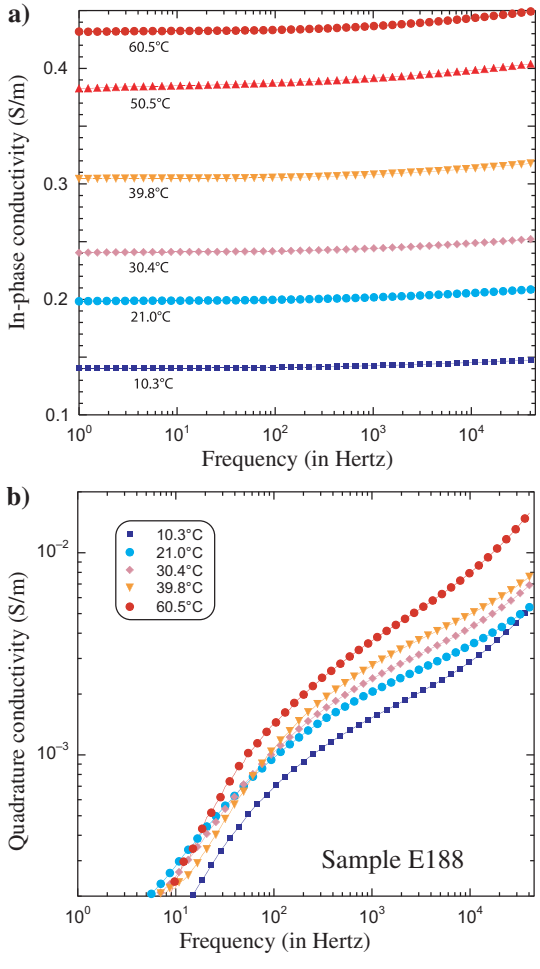


Figure 4. Temperature dependence of the complex conductivity (Sample E188). (a) In-phase conductivity spectra and (b) quadrature conductivity spectra.

## Measurements at different temperatures

The temperature measurements were performed in a temperature-controlled bath using a protocol similar to that of Revil et al. (2018a) (see also Martinez et al., 2012; Hermans et al., 2014; Coperey et al., 2019). The temperatures range from approximately 10°C to 60°C. The maximum temperature of the waste packages in the French concept CIGEO should not exceed 100°C. The French design also implies that the maximum temperature of the surrounding rocks should not exceed 70°C. Consequently, it is highly unlikely that in nominal conditions the bentonite seals will reach temperatures higher than 60°C.

Temperature measurements concern experiments/samples E188, E189, and E190 (see Table 1). The complex conductivity spectra at the different temperatures of sample E188 are shown in Figure 4. We note an increase in the in-phase conductivity and quadrature conductivity with temperature. Because the relaxation times depend on temperature, it is possible that there is a small translation of the spectra with temperature. The samples were indeed wrapped in plastic films. Immediately after compacting the samples, we placed four ECG electrodes on the samples (90° from each other, like in Figure 2 for the measurements at 25°C) that are stable in temperature. We then tightly wrapped each sample and ECG electrodes with a plastic film. We then covered the sample with duct tape to ensure the stability and airtightness of the plastic film around the sample. Finally, we cut the plastic film around the metal ECG snap buttons to allow the electrodes to be connected to the impedance meter and, at the same time, minimize any water loss from the samples. This setup allowed us to connect an alligator clip to each electrode and thus connect each electrode to the impedance meter.

# MODEL

## Equivalent and generalized circuit model

We consider next that a sand-bentonite mix corresponds to a time-invariant (inside the time-frame of the measurements), isotropic, and homogeneous porous medium with a connected pore network. We summarize in this section the petrophysical model developed in the three previous papers of this series. If there is only one polarization length scale (the smectite grains) in the porous material, according to the equivalent circuit shown in Figure 6, the complex conductivity is given by

$$\sigma*(\omega) = \sigma_\infty - \frac{M_n}{1+(i\omega\tau)^{1/2}}, \tag{1}$$

corresponding to a Cole-Cole model for the complex conductivity with a Cole-Cole exponent of $c = 0.5$. In equation 1, $\omega = 2\pi f$ denotes the pulsation frequency, $f$ is the frequency (Hertz), $i$ is the pure imaginary number ($i^2 = -1$), $\sigma_\infty$ (S m$^{-1}$) denotes the instantaneous conductivity (obtained at a high frequency), $\sigma_0$ (S m$^{-1}$) denotes the direct current conductivity (obtained at low frequencies), $M_n$ (S m$^{-1}$) denotes the normalized chargeability ($M_n \equiv \sigma_\infty - \sigma_0$), and $\tau = a^2/2D$ denotes the relaxation time (in s) associated with the depolarization of the polarization length scales by electrodiffusion of the charge carriers ($D$ is the diffusion coefficient of the counterions in the Stern layer and $a$ is a particle size). The rationale for the choice of a Warburg impedance to represent the charge storage of the dynamic Stern layer is that the Stern layer coating the surface

of the clay particles is considered to be a leaking capacitance (see Revil et al., 2014a, 2017, for further explanations). This leaking effect is due to the sorption/desorption effect at the edge of the clay particle in an electrical field (Rosen and Saville, 1991).

The situation is, however, more complicated than portrayed in Figure 6. Indeed, clay minerals tend to form a variety of multiscale structures, such as clay platelets, tectoids, and aggregates (see Dor et al., 2020, and Figure 7). Therefore, equation 2 needs to be generalized to

$$\sigma*(\omega) = \sigma_\infty - M_n \int_0^\infty \frac{h(\tau)}{1+(i\omega\tau)^{1/2}} d\tau, \qquad (2)$$

where $h(\tau)$ denotes a (normalized) probability density for the relaxation times $\tau$ (in s) of the material (e.g., Tarasov and Titov, 2007). If the polarization length scales are very broad, the parametric model describing the complex conductivity spectra is a constant-phase angle (CPA) model resulting from the superposition of the Warburg models over different scales (Revil et al., 2017). This is the case, for instance, in which the heterogeneities are described by power law distributions (for instance, in the case of a fractal porous medium). A future contribution will deal with the clay-rich porous media with a pore space characterized by a fractal dimension. The spectra observed in the present paper are close to constant-phase angle spectra, and therefore, it is possible to extract information on a characteristic time scale $\tau$.

## Sand-bentonite mixes

By adding sand grains to bentonite, we add another polarization length scale to the problem. However, because of its size (approximately 250 μm) and charge density, the Fontainebleau sand polarizes weakly at quite low frequencies (<1 Hz, see Revil et al., 2014a), whereas clay aggregates polarize at high frequencies (>10 Hz). In the present study, we consider the complex conductivity spectra above 1 Hz, and the polarization of the sand grains can be safely neglected. That said, it still has a small effect by decreasing the current density associated with the bentonite itself by reducing its volumetric density. This effect is a mere multiplication of the conductivities and normalized chargeability by a factor $\varphi_{Sd}^{1.5}$ (see Revil, 2000), in which $\varphi_{Sd}$ denotes the volume fraction of sand. This correction factor, being relatively small, will be neglected hereinafter.

## Relationship to the water content and CEC

Assuming that the first and second Archie's exponents are equal, the dynamic Stern layer model yields the following expressions (Revil et al., 2017):

$$\sigma_\infty = \theta^m \sigma_w + \theta^p \rho_g B \mathrm{CEC}_B, \qquad (3)$$

$$\sigma_0 = \theta^m \sigma_w + \theta^p \rho_g (B-\lambda) \mathrm{CEC}_B, \qquad (4)$$

$$M_n = \theta^p \rho_g \lambda \, \mathrm{CEC}_B, \qquad (5)$$

where $\sigma_w$ (S m$^{-1}$) denotes the pore water conductivity (outside the electrical double layer), $\mathrm{CEC}_B$ (in C kg$^{-1}$) denotes the CEC of pure bentonite ($\mathrm{CEC}_B$ of 81.9 ± 0.64 cmol(+)/kg, i.e., 81.9 meq/100 g, 1 meq/100 g = 963.20 C kg$^{-1}$ in SI units), $\theta = s_w \phi$ denotes the (volumetric) water content (dimensionless), $s_w$ (dimensionless) denotes the saturation, $\phi$ (dimensionless) denotes the porosity, $\rho_g$ denotes the grain density (2770 kg m$^{-3}$ for smectite and 2650 kg m$^{-3}$ for silica), $B$ (in m$^2$ s$^{-1}$ V$^{-1}$) denotes the apparent mobility of the counterions for surface conduction, and $\lambda$ (in m$^2$ s$^{-1}$ V$^{-1}$) denotes the apparent mobility of the counterions for the polarization associated with the quadrature conductivity (see Vinegar and Waxman, 1984). The exponent $p>1$ is a saturation exponent for the normalized chargeability (Schmutz et al., 2010). From our previous studies, we obtained $B(\mathrm{Na^+}, 25°\mathrm{C}) = 3.1 \pm 0.3 \times 10^{-9}$ m$^2$s$^{-1}$ V$^{-1}$ and $B(\mathrm{Na^+}, 25°\mathrm{C}) = 3.0 \pm 0.7 \times 10^{-10}$ m$^2$s$^{-1}$ V$^{-1}$ (see, for instance, Revil et al., 2017). A dimensionless number $R$ was introduced by Revil et al. (2017) as $R = \lambda/B \approx 0.10 \pm 0.02$ independent of temperature and saturation. This ratio is also equal to the ratio between the instantaneous surface conductivity (i.e., the last term of equation 3, $\sigma_S^\infty = \theta^p \rho_g B \, \mathrm{CEC}$) and the normalized chargeability given by equation 5 (see discussions in Weller et al. [2013], Revil et al. [2017], and pore scale upscaling using impedance network modeling by Maineult et al. [2017, 2018]). The physical meaning of the exponents $m$ and $p$ is discussed in various papers (see Qiang et al., 2024 and the references therein).

## Relationship between the quadrature conductivity and the normalized chargeability

As mentioned previously, clay-rich media are multiscale materials and, therefore, characterized by a hierarchical structure of polari-

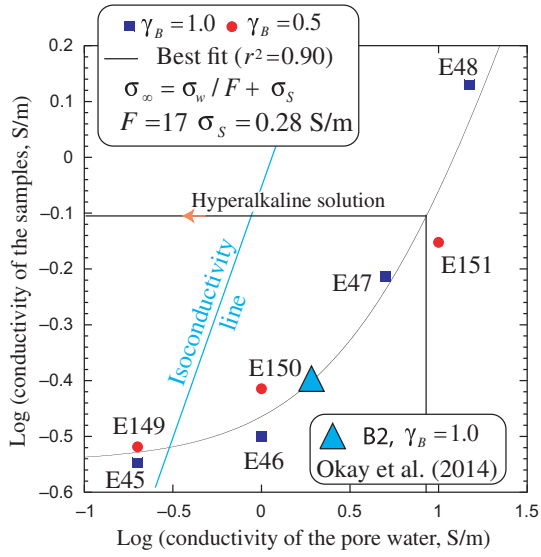


Figure 5. The conductivity of samples at saturation and at a porosity of approximately 0.57 ± 0.02. Here, $\gamma_B$ denotes the bentonite content as a weight fraction. The surface conductivity and formation factor are calculated with the best fit of the linear conductivity equations displayed in the figure ($R^2$ = 0.95). We obtain a surface conductivity of 0.28 S m$^{-1}$ and a formation factor of $F$ = 17 ± 2. The conductivity of sample E75 (saturated with deionized water and characterized by the same porosity of 0.54) allows us to obtain a pore water conductivity value of 0.275 S m$^{-1}$ for the other samples. The samples E45, E46, E47, and E48 are from the study of El Alam et al. (2023) for pure bentonite. The blue-filled triangle corresponds to Bentonite B2 from Okay et al. (2014) (CEC = 44.2 meq/100 g). The isoconductivity line corresponds to the lines for which the conductivity of the sample is equal to the conductivity of the pore water.

zation length scales. Considering the quadrature conductivity at the geometric mean frequency of two frequencies, $f_1$ and $f_2$, and the normalized chargeability defined as the difference between the in-phase conductivity at the frequency $f_2 (> f_1)$ and the in-phase conductivity at the lower frequency $f_1$, the quadrature conductivity and the normalized chargeability can be related to each other by (Van Voorhis et al., 1973)

$$\sigma''\left(\sqrt{f_1 f_2}\right) \approx -\frac{M_n(f_1, f_2)}{\alpha}, \tag{6}$$

where $\alpha \approx (2/\pi) \ln A$ and $A$ denotes the number of decades between $f_1$ and $f_2$ (for instance, for four decades, e.g., 10 Hz and 10 kHz, we have $A = 10^3$ and $\alpha \approx 4.4$). In Figure 8, we see a test on our data set (at a constant temperature and for different temperatures), which confirms the prediction of equation 6. In other words, it is always important to remember that the polarization can be quantified either from the quadrature conductivity or from the dispersion (frequency dependence) of the in-phase conductivity. Equation 6 is rigorously valid in the context of the CPA model and remains a very good approximation even if this assumption is not obeyed but the probability distribution $h(\tau)$ in equation 2 is very broad (Revil et al., 2017).

If the normalized chargeability is not determined between two frequencies but through the entire spectrum (for instance, in equation 5), we have

$$M_n(\infty, 0) \equiv \sigma_\infty - \sigma_0 < M_n(f_1, f_2). \tag{7}$$

The largest value that can be reached by $\alpha$ depends on the ratio of the smallest to the largest polarization length scales that are present in the porous material. For instance, if we assume that the smallest and largest polarization length scales are 0.02 μm (smectite) and 200 μm (sand grains), respectively, i.e., four orders of magnitude, then the associated relaxation times cover eight decades, and the largest value of $\alpha$ given by $\alpha \approx (2/\pi) \ln A$ is $\alpha \approx 8$. This value is of paramount importance to convert the quadrature conductivity to the normalized chargeability $M_n(\infty, 0)$.

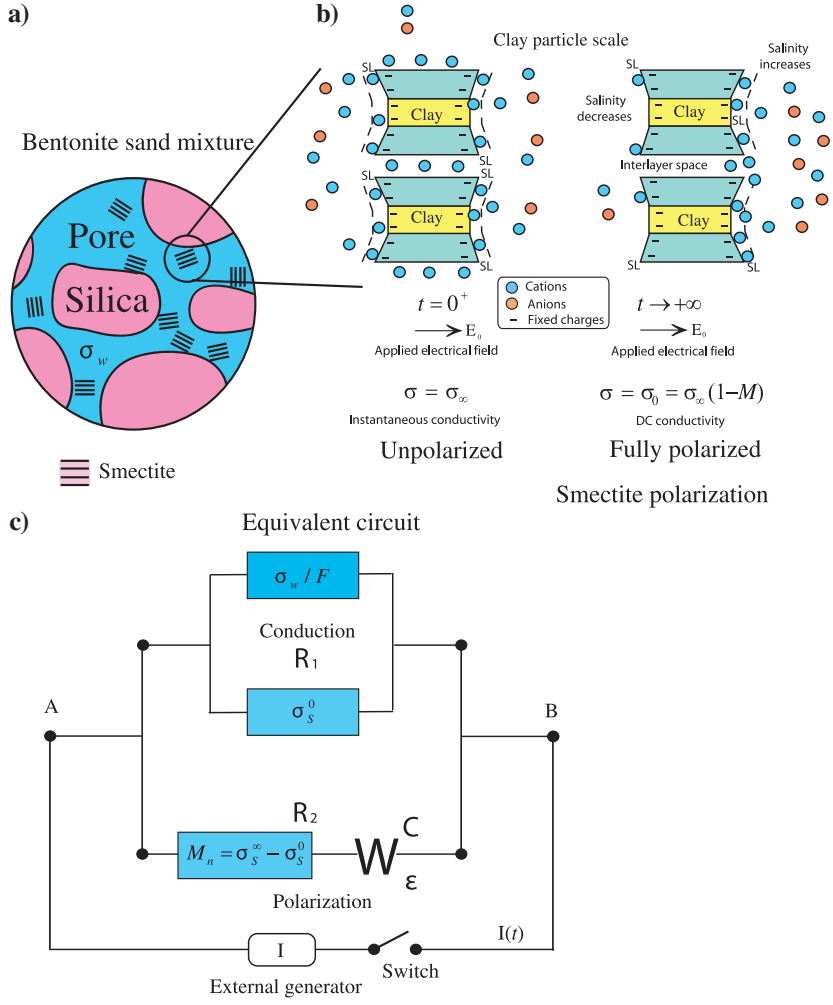


Figure 6. Polarization of a sand-bentonite mixture. (a) The presence of smectite in the mixture would polarize at high frequencies because of their small sizes. They are the first grains to become fully polarized in an applied electrical field. The polarization associated with the silica grain (Fontainebleau sand) is negligible. (b) For a single smectite particle, the polarization of the grain is associated with the migration of the charge carriers (including in the interlayer pore space) under the influence of the applied electrical field (the thermodynamic is actually associated with the electrochemical potential gradient of the charge carriers). The polarization is mainly associated with the Stern layer. (c) The equivalent electrical circuit with a resistance $R_1$ in parallel with a resistance $R_2$ in a series with a leaking (Warburg-type) capacitance C. The presence of the electrical double-layer coating the surface of the grains has an effect on conduction and directly controls the occurrence of (induced) polarization.

## Relationship between the dry density and the quadrature conductivity

As mentioned in the "Introduction", dry density is an important parameter to understand the swelling pressure of smectite-rich materials. In saturated conditions, using equations 5 and 7, the quadrature conductivity can be written as

$$\sigma'' = \frac{\theta^p \rho_g \lambda \, \mathrm{CEC}}{\alpha}. \tag{8}$$

Taking the log of the two members of the previous equation yields

$$\log \sigma'' = p \log \phi + \log\left(\frac{\rho_g B \, \mathrm{CEC}_B R}{\alpha}\right). \tag{9}$$

Because the dry density $\rho_d$ (in kg m$^{-3}$) can be written as a function of the porosity as $\rho_d = (1-\phi)\rho_g$ and therefore $\phi = (\rho_g - \rho_d)/\rho_g$, inserting this relationship into equation 9, we obtain

$$\log \sigma'' = p \log\left(\frac{\rho_g - \rho_d}{\rho_g}\right) + \log\left(\frac{\rho_g B \, \mathrm{CEC}_B R}{\alpha}\right). \tag{10}$$

This provides a closed-form equation between the dry density and the quadrature conductivity that will be tested against the experimental data in the next section.

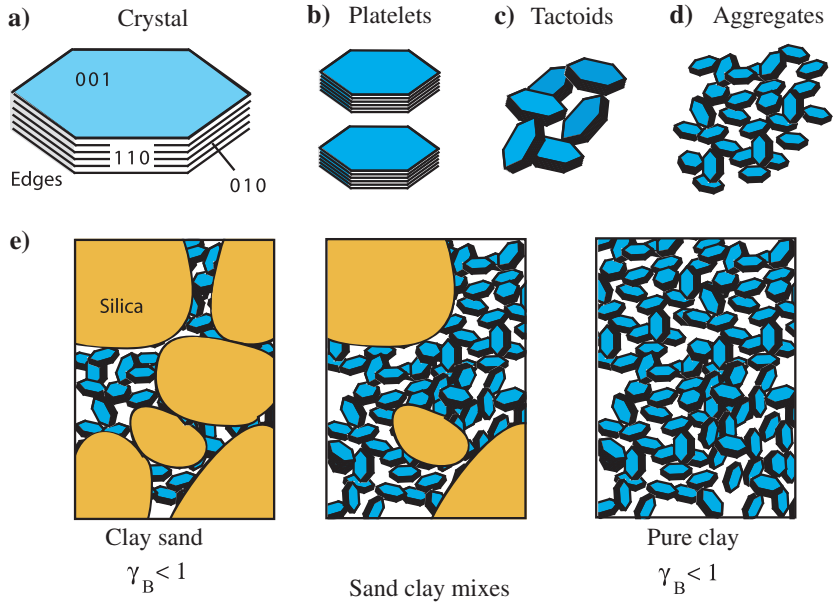


Figure 7. Hierarchical structures in bentonite-sand mixtures. (a) Crystal scale, (b) platelets, (c) tactoids, (d) aggregates, and (e) sand-bentonite mixtures with a bentonite content $\gamma_B$ (weight fraction) comprised between the sand porosity and the pure bentonite end case.

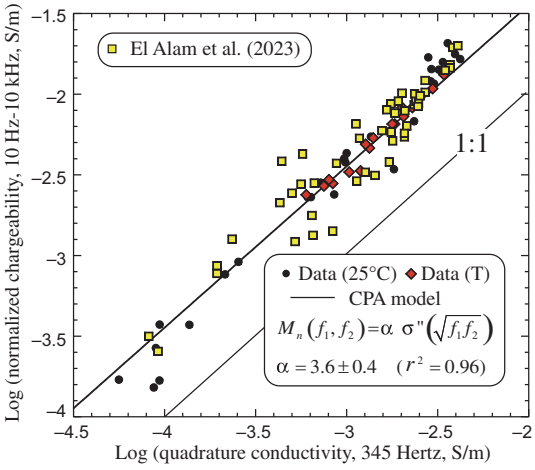


Figure 8. Quadrature conductivity versus normalized chargeability for our data set (measurements at a constant temperature of 25°C and in temperature for samples E188, E189, and E190). We have also added the measurements of El Alam et al. (2023) for the pure bentonite end member. The normalized chargeability is taken as the difference between the in-phase conductivity between $f_1$ = 10 kHz and $f_2$ = 10 Hz, whereas the quadrature conductivity is measured at the geometric mean of the two frequencies. The high frequency range is used to compute the normalized chargeability because the smectite particles are tiny and polarize at high frequencies. The CPA model predicts a slope of $\alpha$ = 4.4, slightly higher than determined from the data themselves ($\alpha = 3.6 \pm 0.4$). In other words, polarization can be determined either through the dispersion of the in-phase conductivity or through the quadrature conductivity.

## RESULTS

### In-phase conductivity

Is surface conductivity the dominant conduction mechanism in our data set? To answer this question, in Figure 9, we plotted the normalized chargeability versus the conductivity for the Table 1 data set. We observed that the samples characterized by high fractions of bentonite are usually characterized by high normalized chargeabilities and conductivity values. They are statistically close to the line with a slope of $R$ = 0.10. This implies that for these samples, the surface conductivity has a strong influence on the overall conductivity. Indeed, the ratio between the normalized chargeability and the conductivity is equal to $R$ only if the surface conductivity dominates the conductivity response of the rock. For sandy samples, the data are characterized by lower normalized chargeabilities and conductivities. The data are rather clustered in the domain for which surface conductivity is more and more negligible. This is an intuitive result that can be quantified here, thanks to such a crossplot.

Figure 10 indicates that the in-phase conductivity follows a power law relationship with saturation. These trends for different bentonite contents are used to determine the in-phase conductivity at saturation (see Table 2). The values at saturation are reported as a function of the bentonite content in Figure 11a. The in-phase conductivity increases with the bentonite content because of the increase of the CEC. This is consistent with the theory (equation 3). In

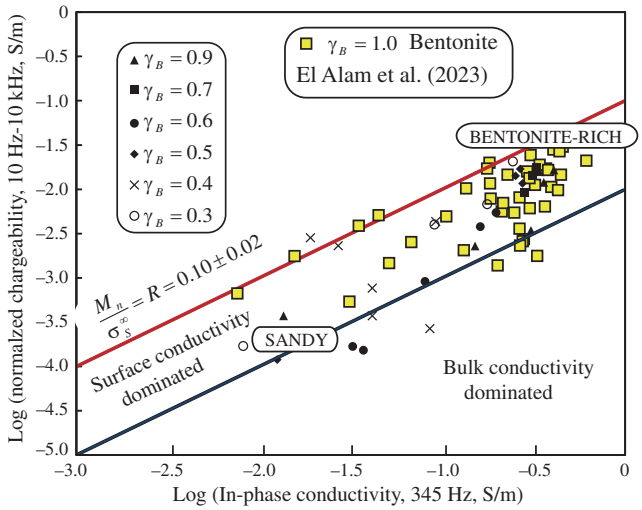


Figure 9. Normalized chargeability versus in-phase conductivity for our data set. The red line represents the slope $R$ = 0.10, which means that the conductivity is dominated along this line by its surface conductivity component. Further below the black line, the conductivity of the mixture is dominated by its bulk component related to the conductivity of the pore water. The red line is the prediction of the dynamic Stern layer model corresponding to a surface conductivity-dominated situation.

Figure 11a, we also report the results of a few experiments performed directly at saturation and the other data points from the literature. They all exhibit the same trend in a consistent way.

In Figure 12, we plot the in-phase conductivity as a function of the water content. We see that the conductivity depends on the water content according to a power law function with an exponent of $m = 2.3$. Thanks to the dynamic Stern layer model, we can predict the values of the prefactor of the scaling law shown in Figure 12. Taking a grain density of $\rho_g = 2650$ kg m$^{-3}$, a mobility $B(\mathrm{Na}^+, 25°\mathrm{C}) = 3.1 \times 10^{-9}$ m$^2$ s$^{-1}$ V$^{-1}$, and the value of the CEC of pure bentonite, $\mathrm{CEC_B} = 90$ meq/100 g $= 87 \times 10^3$ C kg$^{-1}$, we have $\rho_g B\,\mathrm{CEC}_B = 0.75$ S m$^{-1}$. As the pore water conductivity is $\sigma_w = 0.21$ S m$^{-1}$, the prefactor for the in-phase conductivity is $\sigma' = \sigma_0' \theta^{2.3}$ with $\sigma_0' = 1.0$ S m$^{-1}$ for pure bentonite. Figure 12 shows that the prefactor is $\sigma_0' = 1.1 \pm 0.2$ S m$^{-1}$ from the experimental data and is, therefore, in close agreement with the predicted value from the dynamic Stern layer model.

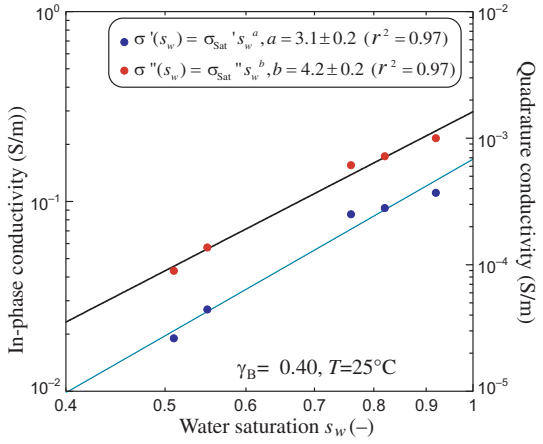


Figure 10. In-phase and quadrature conductivities (at 345 Hz) versus saturation for the same bentonite mass fraction ($\gamma_B$ 0.40). The extrapolation of the trend to $s_w = 1$ allows us to obtain the in-phase or quadrature conductivity values at saturation (a fully water-saturated state). The fits are provided in Table 2.

## Quadrature conductivity

In Figure 11b, we plot the quadrature conductivity as a function of the bentonite content. The quadrature conductivity appears mostly independent of the bentonite content, at least for bentonite contents higher than 30%. This means that the presence of the sand grains (with a very weak polarization) does not affect the polarization of the mixture for bentonite content higher than 0.30. For bentonite content lower than 0.30, the quadrature conductivity decreases with the bentonite content.

In Figure 13, we plot the quadrature conductivity as a function of the water content for the complete collection of data reported in Table 1. We observe a clear power law dependence between the two quantities (as predicted by the model) with a power law exponent $p = 3.3$. This allows fixing the value of this critical parameter for sand-bentonite mixes, which is important for water content monitoring purposes, as discussed subsequently.

Just as for the preceding in-phase conductivity, and thanks to the dynamic Stern layer model, we can predict the values of the prefactor of the scaling law shown in Figure 13. With $\alpha = 8$ (based on the grain size distribution covering four orders of magnitude as discussed previously) and the value of the dimensionless number $R = 0.10$, the prefactor of the power law relationship for the quadrature conductivity is $\sigma_0'' = \rho_g B\,\mathrm{CEC}_B R/a = 0.010$ S m$^{-1}$. The observed prefactor is $\sigma'' = \sigma_0'' \theta^{3.3}$ with $\sigma_0'' = 0.012$ S m$^{-1}$ (see Figure 13), in close agreement with this prediction. We can perform a consistency test with the data shown in Figure 13 at saturation. At a water content of $\theta = 0.6$, the quadrature conductivity is given by $\sigma'' = 0.00242$ S m$^{-1}$, which is again consistent with the value determined from the data in Figure 11b ($\sigma'' = 0.00230$ S m$^{-1}$).

## Effect of temperature

The dependence of complex conductivity on temperature has been the subject of many studies in the literature (for instance, Bairlein et al., 2016). In Figure 14, we plot the in-phase conductivity at 345 Hz as a function of the temperature for three samples characterized by three bentonite contents. The observed dependence on temperature is linear in the temperature range 10°C–60°C and can be written as (Revil et al., 1998; Hayley et al., 2007)

$$\sigma'(T) = \sigma'(T_0)(1 + \alpha_T(T - T_0)), \quad (11)$$

with $\alpha_T = 0.028 \pm 0.001$ /°C and $T_0 = 25$°C. In Figure 15, we plot the quadrature conductivity (at 345 Hz) and the normalized chargeability (taken as the difference between the in-phase conductivity between 10 Hz and 10 kHz) as a function of the temperature. The data can also be fitted as a function of the temperature by a linear law similar to equation 8 with $\alpha_T = 0.021 \pm 0.002$ /°C and $T_0 = 25$°C. We observe, therefore, that the temperature dependence of the quadrature conductivity (and normalized chargeability) is slightly smaller than for the in-phase conductivity. As explained previously, we cannot fit the spectra with a Cole-Cole model as the spectra are better described by a CPA model. Therefore, we are unable to show the temperature dependence of the relaxation time.

**Table 2. Parameters determined from the best fit between the in-phase and quadrature conductivities versus the saturation for different values of the bentonite mass fraction $\gamma_B$.**

| $\gamma_B$ | $\sigma'$ ($s_w = 1$) | $a$ | $\sigma''$ ($s_w = 1$) | $b$ | $M_n''$ ($s_w = 1$) |
|---|---|---|---|---|---|
| 1.0 | 0.438 | — | 0.0020 | — | 0.16 |
| 0.9 | 0.397 | 3.46 ± 0.17 | 0.0029 | 4.07 ± 0.32 | 0.023 |
| 0.7 | 0.306 | 2.18 ± 0.21 | 0.0029 | 3.96 ± 0.34 | 0.023 |
| 0.6 | 0.217 | 2.59 ± 0.23 | 0.0015 | 4.01 ± 0.23 | 0.012 |
| 0.5 | 0.257 | 3.70 ± 0.14 | 0.0029 | 5.63 ± 0.21 | 0.023 |
| 0.4 | 0.168 | 3.11 ± 0.21 | 0.0017 | 4.22 ± 0.21 | 0.013 |
| 0.3 | 0.166 | 3.63 ± 0.12 | 0.0020 | 3.43 ± 0.28 | 0.016 |

Note: For the experiment performed at full saturation ($\gamma_B = 1$), we use sample E28 from El Alam et al. (2023). The data are fitted by the following expressions: $\sigma'(s_W) = \sigma'(s_W = 1)\, s_W{}^a$ and $\sigma''(s_W) = \sigma''(s_W = 1)\, s_W{}^b$. The mean values for $a$ and $b$ are $a = 3.2 \pm 0.6$ and $b = 4.2 \pm 0.7$. The normalized chargeability over the full spectra is obtained from the quadrature conductivity at saturation times $\alpha = 8$.

## Relationship to the dry density

In Figure 16, we plot the quadrature conductivity versus the dry density $\rho_d$ (at a constant temperature), and we observe a relationship consistent with the form of equation 10 using the same input parameters for the Stern layer as discussed previously. This shows the predictive ability of the dynamic Stern layer model to capture such a data trend.

## Comparison with other data sets

We now discuss the consistency of the results obtained for bentonite with the other data sets of soils and volcanic rocks that are also rich in smectite. Figure 17 shows Archie's law (that is, the relationship between the formation factor and the porosity) for a collection of rock samples rich in smectite. We choose mostly volcanic rocks, for which the smectite content is associated with the alteration of the volcanic glasses. As we can see in Figure 17, bentonite

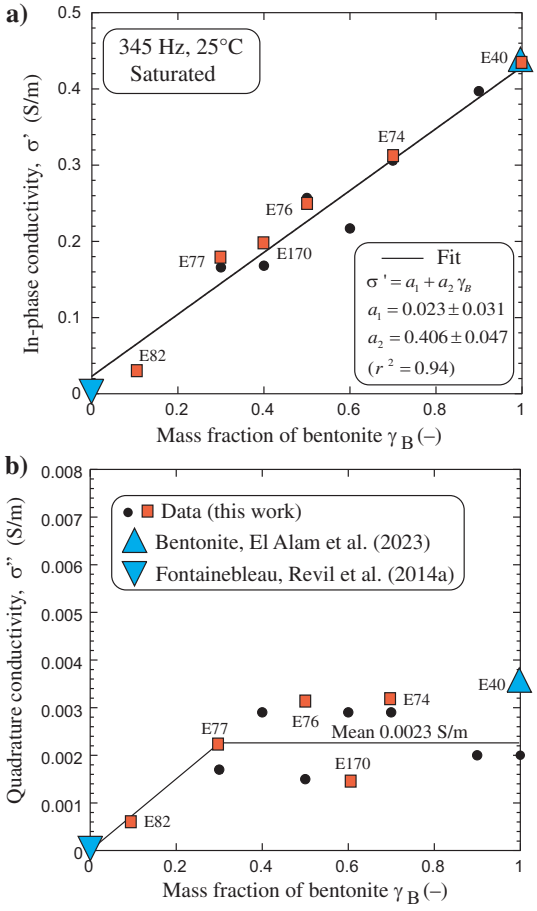


Figure 11. Influence of the mass fraction of bentonite at saturation. (a) In-phase conductivity at saturation versus the bentonite content by weight $\gamma_B$. Because $\gamma_B$ is dimensionless, $a_1$ and $a_2$ are expressed in S m$^{-1}$. (b) Quadrature conductivity at saturation versus the bentonite content by weight $\gamma_B$. The black circles correspond to the extrapolated value from the trends shown in Figure 9. The red-filled squares correspond to some of the experiments made with deionized water at full saturation. The blue triangle corresponds to sample E40 (porosity 0.68, fully saturated) from the study of El Alam et al. (2023). Both data sets show some scattering in the values around a mean value with no clear trends.

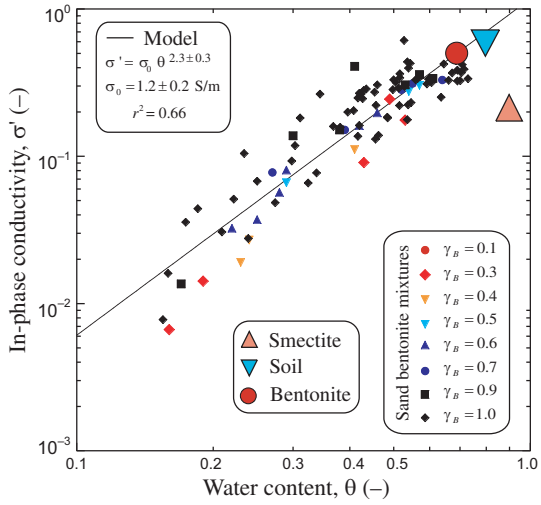


Figure 12. In-phase conductivity (345 Hz, 25°C) versus the water content by volume for the entire collection of experiments provided in Table 1 (saturated and unsaturated samples). The data from the study of El Alam et al. (2023) have been added for the pure bentonite samples ($\gamma_B$ = 1). The power law fit is used to obtain the value of the exponent. Assuming that the bentonite conductivity is dominated by surface conductivity with a power law exponent equal to $m$-1, we obtain $m$ = 3.3 ± 0.3. The pure smectite data point (very high porosity of the gel of 0.90) is from Revil et al. (2018b). The soil is the CG soil sample from the study of Revil et al. (2017) (porosity 0.78, CEC = 19 meq/100 g). The bentonite corresponding to the large red circle is sample B2 from Okay et al. (2014) (porosity 0.67, CEC = 44.2 meq/100 g).

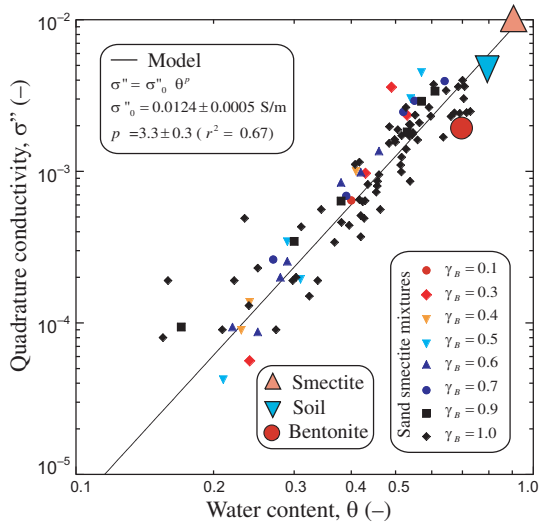


Figure 13. Quadrature conductivity (345 Hz, 25°C) versus the water content by volume for the entire collection of experiments provided in Table 1 (saturated and unsaturated samples). The data from the study of El Alam et al. (2023) have been added for the pure bentonite samples ($\gamma_B$ = 1). The power law fit is used to obtain the value of the exponent $p$. The pure smectite data point (porosity 0.90, fully saturated) is from Revil et al. (2018). The soil is the CG soil sample from the study of Revil et al. (2017) (porosity 0.78, CEC 19 meq/100 g). The bentonite corresponding to the large red circle is sample B2 from Okay et al. (2014) (porosity 0.67, CEC = 44.2 meq/100 g).

data (from Figure 4) are consistent with the large data set shown in this figure with a cementation/porosity exponent $m = 2.2$ consistent with the trend discussed previously in Figure 12 between the in-phase conductivity and the water content.

In Figure 18, we plot a broad data set of experimental data in terms of surface conductivity versus the reduced CEC, defined as the CEC divided by the bulk tortuosity of the pore space (that is, the product of the formation factor by the porosity; see the last term of equation 3). Here again, the bentonite data (saturated bentonite, see Figure 4) show great consistency with the data set of rocks rich in smectite being, as expected, an end member in the trend.

The result is even more striking in Figure 19, wherein we plot the normalized chargeability versus the surface conductivity. The slope of the trend corresponds to the dimensionless number $R$ discussed previously. The data are consistent with the value $R = 0.10$, as discussed previously. We can, therefore, conclude that bentonite is really an end member of smectite-rich porous media, and the properties of bentonite are consistent with published data for rocks and soils that are rich in smectite.

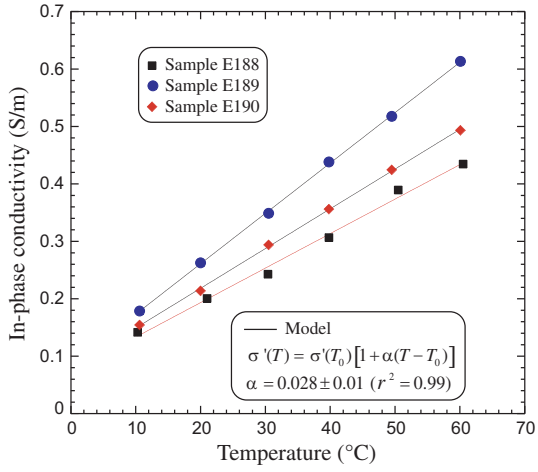


Figure 14. In-phase conductivity (in S m$^{-1}$) versus the temperature (in °C) for three samples characterized by different bentonite contents $\gamma_B$. The reference temperature is $T_0$ = 25°C. Sample E188, $\sigma'(T_0) = 0.223 \pm 0.005$ S m$^{-1}$. Sample E189, $\sigma'(T_0) = 0.305 \pm 0.001$ S m$^{-1}$. Sample E190, $\sigma'(T_0) = 0.253 \pm 0.002$ S m$^{-1}$.

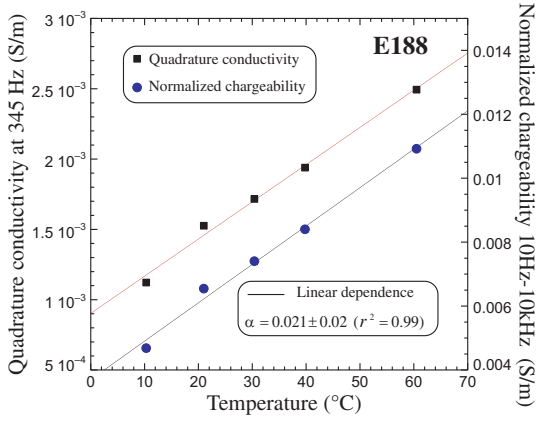


Figure 15. Quadrature conductivity and normalized chargeability (in S m$^{-1}$) versus the temperature (in °C) for Sample E188. The reference temperature is $T_0$ = 25°C. As expected, the quadrature conductivity and the normalized chargeability have the same temperature dependence.

## DISCUSSION

There are two questions we want to tackle in this discussion. The first is related to the potential application of IP to monitor bentonite seals in the context of DGDs. We can perform frequency- or time-domain IP measurements to image, in 3D, the conductivity and normalized chargeability at different times (going from one domain to the other is done through a mere Fourier transform). We know the conductivity of the pore water from chemical modeling (possibly including the effects of alkalinity associated with the presence of cement) and the effect of temperature, thanks to the results shown in the present paper. This would require, however, determining the relationship between the normalized chargeability determined for a given period of current injection (by default 1 s) and the normalized chargeability covering the entire spectrum $M_n(\infty, 0)$, as discussed previously. A correction factor (>1) should be applied to the inverted normalized chargeability data, and we will develop some relationships to determine this correction factor. Then, for each pixel describing a 3D tomogram, we have two dynamic results, namely the conductivity and the normalized chargeability. From these two measurements, we can determine the water content and CEC at each time step. If the clay mineralogy remains the same, only the water content is expected to change over time. However, if the pH changes, we can observe the illitization of the smectite in the presence of potassium, leading, in turn, to a change in the CEC over time (this process is discussed in the next paper of this series; see El Alam et al., 2024).

The second question of interest is what could be done to improve our model. First, we should extend the frequency domain to a higher

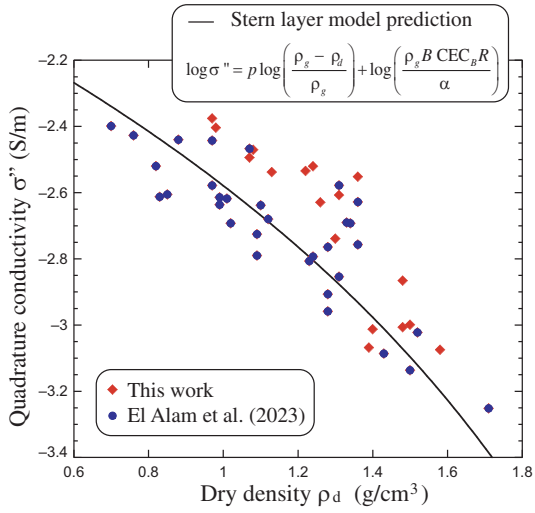


Figure 16. Quadrature conductivity (345 Hz, 25°C) versus the dry density (saturated and nearly saturated samples with saturation >0.90). Data from the study of El Alam et al. (2023) have been added ($\gamma_B = 1$), also using only the saturated sample. The black line corresponds to the dynamic Stern layer model with a quadrature conductivity exponent $p$ = 3.3, a grain density $\rho_g = 2650$ kg m$^{-3}$, $B(Na^+, 25°C) = 3.1 \times 10^{-9}$ m$^2$s$^{-1}$ V$^{-1}$, $CEC_B = 90$ meq/100 g = $87 \times 10^3$ C kg$^{-1}$, $R = 0.10$, and $\alpha = 8$ as discussed in the main text.

DOI:10.1190/geo2024-0110.1

frequency (perhaps 10 MHz) to be sure we can fit the complex conductivity spectra to account for double-layer polarization and Maxwell-Wagner polarization (see De Lima and Sharma, 1992).

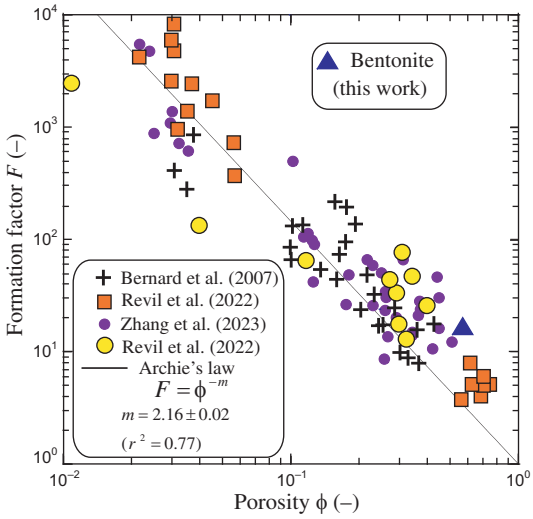


Figure 17. The relationship between the formation factor and the connected porosity using Archie's law. The fit of Archie's law (Archie, 1942) for the data set. We have also provided the data from the recent study of Revil et al. (2022) using 10 additional core samples from the same volcano and core sample data from another stratovolcano, the Papandayan, in Indonesia, from the study of Revil et al. (2022). The data from the La Montagne Pelée volcano (Martinique Island, France) are from Bernard et al. (2007), with the exception of the pumices. The work of Zhang et al. (2023) concerns the La Soufrière volcano, Guadeloupe Island. The blue triangle corresponds to the present work ($F$ = 17, $\phi$ = 0.57).

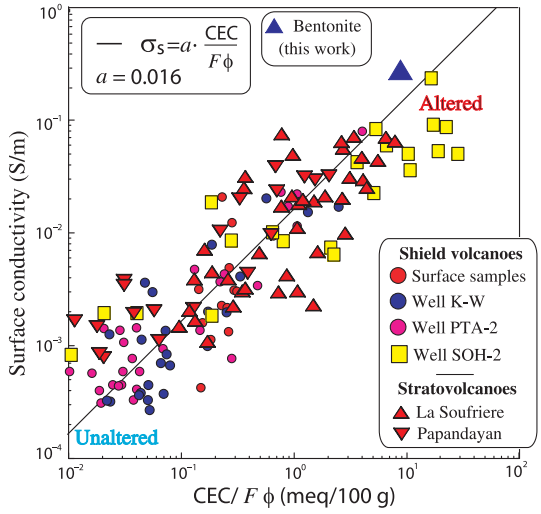


Figure 18. Dependence of surface conductivity (S m$^{-1}$) with the CEC (in meq/100 g, 1 meq /(100 g) = 963.2 C kg$^{-1}$) divided by the bulk tortuosity of the pore space (product of the formation factor with the connected porosity). There are 135 core samples from volcanoes in the plot, including the 41 samples from the study by Zhang et al. (2023) and the La Soufrière stratovolcano in Guadeloupe Island. The slope is equal to $B\,\rho_g$. The data set includes various data from the Kilauea Shield volcano (Hawaii; see Zhang et al., 2023 for details). For the bentonite sample, $F$ = 17, $\sigma_S = 0.28$ S m$^{-1}$, and the CEC is 82 meq/100 g (MX80).

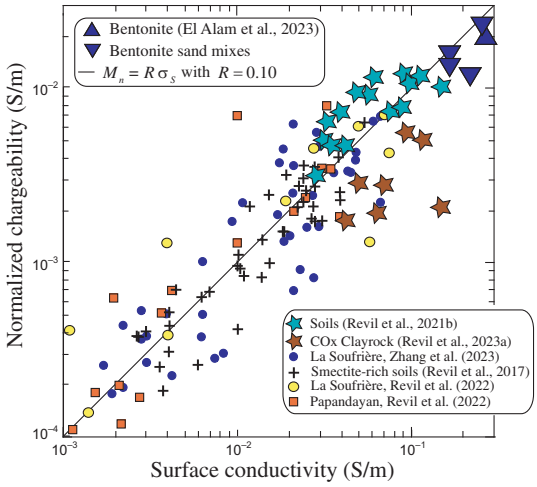


Figure 19. Relationship between the normalized chargeability and the surface conductivity $\sigma_S$. The ratio between the two parameters is equal to the dimensionless parameter $R = \lambda/B \approx 0.10$. The data set includes data from the La Soufrière volcano (see Revil et al., 2022 and Zhang et al., 2023) and the Papandayan stratovolcanoes from Revil et al. (2022), and the smectite-rich soils from Revil et al. (2017). The COx clayrock data are from Revil et al. (2023a), whereas the soil data are from Revil et al. (2021b). The data for the fully saturated bentonite correspond to $\sigma_S$ = 0.28 S m$^{-1}$ and $M_n$ = 0.02 S m$^{-1}$. The sand-bentonite mixtures are taken from Table 2 (values at saturation and assuming that the conductivity is close to the surface conductivity at low salinity for high clay contents).

The second point would be to modify our model to account for the dual water, such as the bulk pore water and the hydration water, as done by Clavier et al. (1984). The third ingredient would be to consider a surface Archie's law for the surface conductivity and the quadrature conductivity/normalized chargeability (see preliminary work by Wang and Revil [2020], for surface conductivity in fractal-type porous media). Such an extension will be developed in a future paper of this series (Part 7).

## CONCLUSION

In the previous papers of this series, we have been dealing with the effect of desiccation in anisotropic clay rocks and the influence of pyrite in illite-pyrite mixtures upon the complex conductivity of such clayey materials. In the present paper, we have been dealing with the effect of saturation and the weight fraction of sand in sand-bentonite mixtures. This opportunity offers another way to test the predictions and limits of the dynamic Stern layer model we have developed in this series of papers.

To reach this goal, we performed 42 new experiments to investigate the effect of the water content on the complex conductivity of sand-bentonite mixtures that can be used as seals for the storage of high-level, long-lived radioactive wastes in underground repositories. At a given saturation, the in-phase conductivity linearly depends on the bentonite content because of the increase of the CEC with the amount of smectite. The quadrature conductivity and the normalized chargeability are independent of the mass fraction of bentonite (at least for mass fractions higher than 10%).

The in-phase and quadrature conductivities depend on the water content according to power law relationships, with a power law exponent of $m$ = 2.3 for the in-phase conductivity and $p$ = 3.3 for the quadrature conductivity. The in-phase and quadrature conductivities

DOI:10.1190/geo2024-0110.1

linearly depend on temperature in the temperature range of 10°C–60°C with a coefficient of 2.1%/°C to 2.8%/°C. When compared with other clay-rich material, the bentonite and bentonite-sand mixtures appear as an end member because of the very high CEC of smectite. This work illustrates the usefulness of the spectral IP method because of its sensitivity to changes in water content in complex media such as sand-bentonite mixtures. The model could be used to interpret field data in a wide variety of contexts, including for volcanoes and landslides.

## ACKNOWLEDGMENTS

We thank the editor, M. Sen, the associate editor, and four anonymous reviewers for their constructive comments regarding our manuscript. This work is cofunded by the Institut de Radioprotection et de Sûreté Nucléaire (IRSN) and by the European Union within the MODATS program.

## DATA AND MATERIALS AVAILABILITY

Data associated with this research are confidential and cannot be released.

## REFERENCES

Archie, G. E., 1942, The electrical resistivity log as an aid in determining some reservoir characteristics: Transactions of the AIME, **146**, 54–62.
Atekwana, E. A., and L. D. Slater, 2009, Biogeophysics: A new frontier in Earth science research: Reviews of Geophysics, **47**, RG4004, doi: 10.1029/2009RG000285.
Bairlein, K., M. Bücker, A. Hördt, B. Hinze, and S. Nordsiek, 2016, Temperature dependence of spectral induced polarization data: Experimental results and membrane polarization theory: Geophysical Journal International, **205**, 440–453, doi: 10.1093/gji/ggw027.
Bairlein, K., A. Hördt, and S. Nordsiek, 2014, The influence of the sample preparation on induced polarization spectra of unconsolidated sediments: Near Surface Geophysics, **12**, 667–678, doi: 10.3997/1873-0604.2014023.
Bardelli, F., C. Mondelli, M. Didier, J. G. Vitillo, D. R. Cavicchia, J.-C. Robinet, L. Leone, and L. Charlet, 2014, Hydrogen uptake and diffusion in Callovo-Oxfordian clay rock for nuclear waste disposal technology: Applied Geochemistry, **49**, 168–177, doi: 10.1016/j.apgeochem.2014.06.019.
Barreto, A. N., and C. A. Dias, 2014, Fluid salinity, clay content, and permeability of rocks determined through complex resistivity partition fraction decomposition: Geophysics, **79**, no. 5, D333–D347, doi: 10.1190/geo2013-0306.1.
Bernard, M.-L., M. Zamora, Y. Géraud, and G. Boudon, 2007, Transport properties of pyroclastic rocks from Montagne Pelée volcano (Martinique, Lesser Antilles): Journal of Geophysical Research: Solid Earth, **112**, B05205, doi: 10.1029/2006JB004385.
Bertrand, J., M. Morosini, J.-L. Garcia-Sineriz, J. Verstricht, and A. Bergmans, 2019, Development and demonstration of monitoring strategies and technologies: Modern2020 report No. 19317 of the WM2019: 45, Annual Waste Management Conference.
Biryukov, A., N. Tisato, and G. Grasselli, 2016, Attenuation of elastic waves in bentonite and monitoring of radioactive waste repositories: Geophysical Journal International, **205**, 105–121, doi: 10.1093/gji/ggv548.
Bourbié, T., and B. Zinszner, 1985, Hydraulic and acoustic properties as a function of porosity in Fontainebleau Sandstone: Journal of Geophysical Research: Solid Earth, **90**, 11524–11532, doi: 10.1029/JB090iB13p11524.
Bradbury, M. H., and B. Baeyens, 2003, Porewater chemistry in compacted re-saturated MX-80 bentonite: Journal of Contaminant Hydrology, **61**, 329–338, doi: 10.1016/S0169-7722(02)00125-0.
Breede, K., A. Kemna, O. Esser, E. Zimmermann, H. Vereecken, and J. A. Huisman, 2012, Spectral induced polarization measurements on variably saturated sand-clay mixtures: Near Surface Geophysics, **10**, 479–489, doi: 10.3997/1873-0604.2012048.
Chapman, N., 2006, Geological disposal of radioactive wastes: Concept, status and trends: Journal of Iberian Geology, **32**, 7–14.
Chen, Y.-G., Y.-J. Cui, A. M. Tang, Q. Wang, and W.-M. Ye, 2014, A preliminary study on hydraulic resistance of bentonite/host-rock seal interface: Géotechnique, **64**, 997–1002, doi: 10.1680/geot.13.P.209.
Cho, W. J., J. O. Lee, and C. H. Kang, 2000, Hydraulic conductivity of bentonite-sand mixture for a potential backfill material for a high-level radioactive waste repository: Journal of the Korean Nuclear Society, **32**, 495–503.
Clavier, C., G. Coates, and J. Dumanoir, 1984, Theoretical and experimental bases for the dual-water model for interpretation of shaly sands: SPE Journal, **24**, 153–168, doi: 10.2118/6859-PA.
Coperey, A., A. Revil, and B. Stutz, 2019, Electrical conductivity versus temperature in freezing conditions: A field experiment using a basket geothermal heat exchanger: Geophysical Research Letters, **46**, 14531–14538, doi: 10.1029/2019GL084962.
Cosenza, P., A. Ghorbani, N. Florsch, and A. Revil, 2007, Effects of drying on the low-frequency electrical properties of Tournemire argillites: Pure and Applied Geophysics, **164**, 2043–2066, doi: 10.1007/s00024-007-0253-0.
Cosenza, P., A. Ghorbani, A. Revil, M. Zamora, M. Schmutz, D. Jougnot, and N. Florsch, 2008, A physical model of the low-frequency electrical polarization of clay-rocks: Journal of Geophysical Research: Solid Earth, **113**, B08204, doi: 10.1029/2007JB005539.
Cui, Y. J., A. M. Tang, C. Loiseau, and P. Delage, 2008, Determining the unsaturated hydraulic conductivity of a compacted sand–bentonite mixture under constant-volume and free-swell conditions: Physics and Chemistry of the Earth, Parts A/B/C, **33**, S462–S471, doi: 10.1016/j.pce.2008.10.017.
Darde, B., A. M. Tang, J.-M. Pereira, P. Dangla, J.-N. Roux, B. Chabot, J. Talandier, and M. Ngoc Vu, 2022, Influence of heterogeneities of density on the hydromechanical behaviour of pellet-based bentonite materials in imbibition experiments: Applied Clay Science, **216**, 106353, doi: 10.1016/j.clay.2021.106353.
De Carvalho Faria Lima Lopes, B., C. Sachet, P. Sentenac, V. Benes, P. Dick, J. Bertrand, and A. Tarantino, 2019, Preliminary non-intrusive geophysical electrical resistivity tomography surveys of a mock-up scale monitoring of an engineered barrier system at URL Tournemire: The Geology Society of London, **482**, 331–345, doi: 10.1144/SP482.11.
Delage, P., Y. J. Cui, and A.M. Tang, 2010, Clays in radioactive waste disposal: Journal of Rock Mechanics and Geotechnical Engineering, **2**, 111–123, doi: 10.3724/SP.J.1235.2010.00111.
De Lima, O. A. L., and M. M. Sharma, 1992, A generalized Maxwell-Wagner theory for membrane polarization in shaly sands: Geophysics, **57**, 431–440, doi: 10.1190/1.1443257.
Dieudonné, A.-C., C. Gatabin, J. Talandier, F. Collin, and R. Charlier, 2016, Water retention behaviour of compacted bentonites: experimental observations and constitutive model: 3rd European Conference on Unsaturated Soils.
Dixon, D. A., M. N. Gray, and A. W. Thomas, 1985, A study of the compaction properties of potential clay-sand buffer mixtures for use in nuclear fuel waste disposal: Engineering Geology, **21**, 247–255, doi: 10.1016/0013-7952(85)90015-8.
Dor, M., Y. Levi-Kalisman, R. J. Day-Stirrat, Y. Mishael, and S. Emmanuel, 2020, Assembly of clay mineral platelets, tactoids, and aggregates: Effect of mineral structure and solution salinity: Journal of Colloid and Interface Science, **566**, 163–170, doi: 10.1016/j.jcis.2020.01.084.
Doyen, P. M., 1988, Permeability, conductivity, and pore geometry of sandstone: Journal of Geophysical Research: Solid Earth, **93**, 7729–7740, doi: 10.1029/JB093iB07p07729.
Ducut, J. D., M. Alipio, P. J. Go, R. Concepcion, R. R. Vicerra, A. Bandala, and E. Dadios, 2022, A Review of electrical resistivity tomography applications in underground imaging and object detection: Displays, **73**, 102208, doi: 10.1016/j.displa.2022.102208.
Dukhin, S. S., and V. N. Shilov, 1974, Dielectric phenomena and the double layer in disperse systems and polyelectrolytes: John Wiley.
Duvillard, P. A., A. Revil, Y. Qi, A. Soueid Ahmed, A. Coperey, and L. Ravanel, 2018, Three-dimensional electrical conductivity and induced polarization tomography of a rock glacier: Journal of Geophysical Research: Solid Earth, **123**, 9528–9554, doi: 10.1029/2018JB015965.
El Alam, J., A. Revil, and P. Dick, 2023, Influence of the water content on the complex conductivity of bentonite: Engineering Geology, **322**, 107183, doi: 10.1016/j.enggeo.2023.107183.
El Alam, J., A. Revil, and P. Dick, 2024, Induced polarization of clay-rich materials. 5. Influence of hyperalkalinity in bentonite: Geophysics, **89**, no. 6, E267–E279, doi: 10.1190/geo2024-0111.1.
Ewing, R. C., R. A. Whittleston, and B. W. D. Yardley, 2016, Geological disposal of nuclear waste: A primer: Elements, **12**, 233–237, doi: 10.2113/gselements.12.4.233.
Fixman, M., 1980, Charged macromolecules in external fields. I. The sphere: The Journal of Chemical Physics, **72**, 5177–5186, doi: 10.1063/1.439753.
García-Siñeriz, J. L., M. R. Mazón, F. Kober, and T. Sakaki, 2019, Performance of THM monitoring instrumentation in FEBEX bentonite barrier after 18 years of operation under repository-like conditions: Geomechanics for Energy and the Environment, **17**, 75–89, doi: 10.1016/j.gete.2018.09.008.
Gens, A., M. Sánchez, L. N. Guimarães, E. E. Alonso, A. Lloret, S. Olivella, M. V. Villar, and F. Huertas, 2009, A full-scale in situ heating test for high-level nuclear waste disposal: Observations, analysis and interpretation: Géotechnique, **59**, 377–399, doi: 10.1680/geot.2009.59.4.377.

DOI:10.1190/geo2024-0110.1


Grosse, C., 2009, Generalization of a classic theory of the low frequency dielectric dispersion of colloidal suspensions to electrolyte solutions with different ion valences: Journal of Physical Chemistry B, **113**, 11201–11215, doi: 10.1021/jp904742v.

Guillaume, D., 2002, Etude expérimentale du système fer-smectite en présence de solution à 80°C et 300°C: Ph.D. thesis, Université Henri Poincaré - Nancy 1.

Guo, X., S. Gin, and G. S. Frankel, 2020, Review of corrosion interactions between different materials relevant to disposal of high-level nuclear waste: npj Materials Degradation, **4**, 1–16, doi: 10.1038/s41529-020-00140-7.

Hayley, K., L. R. Bentley, M. Gharibi, and M. Nightingale, 2007, Low temperature dependence of electrical resistivity: Implications for near surface geophysical monitoring: Geophysical Research Letters, **34**, 1–5, doi: 10.1029/2007GL031124.

Hermans, T., F. Nguyen, T. Robert, and A. Revil, 2014, Geophysical methods for monitoring temperature changes in shallow low enthalpy geothermal systems: Energies, **7**, 5083–5118, doi: 10.3390/en7085083.

Imbert, C., and M. V. Villar, 2006, Hydro-mechanical response of a bentonite pellets/powder mixture upon infiltration: Applied Clay Science, **32**, 197–209, doi: 10.1016/j.clay.2006.01.005.

Jougnot, D., 2020, Developing hydrogeophysics for critical zone studies, importance of heterogeneities and processes at the mesoscopic scale: Dissertation, HDR (Habilitation à Diriger des Recherches).

Jougnot, D., A. Ghorbani, A. Revil, P. Leroy, and P. Cosenza, 2010, Spectral induced polarization of partially saturated clay-rocks: A mechanistic approach: Geophysical Journal International, **180**, 210–224, doi: 10.1111/j.1365-246X.2009.04426.x.

Kanno, T., and H. Wakamatsu, 1992, Water uptake and swelling properties of unsaturated bentonite buffer materials: Canadian Geotechnical Journal, **29**, 1102–1107, doi: 10.1139/t92-127.

Kruschwitz, S., and U. Yaramanci, 2004, Detection and characterization of the disturbed rock zone in claystone with complex resistivity method: Journal of Applied Geophysics, **57**, 63–79, doi: 10.1016/j.jappgeo.2004.09.003.

Leroy, P., and A. Revil, 2009, A mechanistic model for the spectral induced polarization of clay materials: Journal of Geophysical Research: Solid Earth, **114**, B10202, doi: 10.1029/2008JB006114.

Li, Q., L. Feng, S. D. Cameron, H. W. Deckman, and D. Ertas, 2021, Quantifying the origin of membrane polarization: Geophysical Journal International, **227**, 1004–1011, doi: 10.1093/gji/ggab209.

Lyklema, J., S. S. Dukhin, and V. N. Shilov, 1983, The relaxation of the double layer around colloidal particles and the low-frequency dielectric dispersion. Part 1. Theoretical considerations: Journal of Electroanalytical Chemistry and Interfacial Electrochemistry, **143**, 1–21, doi: 10.1016/S0022-0728(83)80251-4.

Madsen, F. T., 1998, Clay mineralogical investigations related to nuclear waste disposal: Clay Minerals, **33**, 109–129, doi: 10.1180/000985598545318.

Maineult, A., D. Jougnot, and A. Revil, 2018, Variations of petrophysical propetties and spectral induced polarization in response to drainage and imbibition: A study on a correlated random tube network: Geophysical Journal International, **212**, 1398–1411, doi: 10.1093/gji/ggx474.

Maineult, A., A. Revil, C. Camerlynck, N. Florsch, and K. Titov, 2017, Upscaling of spectral induced polarization response using random tube networks: Geophysical Journal International, **209**, 948–960, doi: 10.1093/gji/ggx066.

Manukyan, E., H. Maurer, S. Marelli, S. A. Greenhalgh, and A. G. Green, 2012, Seismic monitoring of radioactive waste repositories: Geophysics, **77**, no. 6, EN73–EN83, doi: 10.1190/geo2011-0420.1.

Martin, T., and T. Günther, 2013, Complex resistivity tomography (CRT) for fungus detection on standing oak trees: European Journal of Forest Research, **132**, 765–776, doi: 10.1007/s10342-013-0711-4.

Marshall, D. J., and T. R. Madden, 1959, Induced polarization, a study of its causes: Geophysics, **24**, 790–816, doi: 10.1190/1.1438659.

Martin, T., K. Kuhn, T. Günther, and R. Kniess, 2020, Geophysical exploration of a historical stamp mill dump for the volume estimation of valuable residues: Journal of Environmental and Engineering Geophysics, **25**, 275–286, doi: 10.2113/JEEG19-080.

Martin, T., A. Weller, and L. Behling, 2022, Desaturation effects of pyrite–sand mixtures on induced polarization signals: Geophysical Journal International, **228**, 275–290, doi: 10.1093/gji/ggab333.

Martinez, F. J., M. L. Batzle, and A. Revil, 2012, Influence of temperature on seismic velocities and complex conductivity of heavy oil-bearing sands: Geophysics, **77**, no. 3, WA19–WA34, doi: 10.1190/geo2011-0433.1.

Maurer, H., E. Manukyan, L. Koskova, M. Hokr, J. Korkealaakso, E. Bohner, B. De Carvalho Faria Lima Lopes, and A. Tarantino, 2019, Geophysical monitoring of high-level radioactive waste repositories: Deliverable 6.3 in Modern2020 Final Conference Proceedings, 2nd International Conference about Monitoring in Geological Disposal of Radioactive Waste.

McCombie, C., D. L. Pentz, M. Kurzeme, and I. Miller, 2000, Deep geological repositories: A safe and secure solution to disposal of nuclear wastes: ISRM International Symposium.

Mckinley, I., R. Alexander, and P. Blaser, 2007, Development of geological disposal concepts: Radioactivity in the Environment, **9**, 41–76, doi: 10.1016/S1569-4860(06)09003-6.

Mendieta Tenorio, A., 2021, Clay characterization using spectral induced polarization: Ph.D. thesis, Sorbonne Université.

Mendonça, C. A., R. Doherty, N. D. Amaral, B. McPolin, M. J. Larkin, and A. Ustra, 2015, Resistivity and induced polarization monitoring of biogas combined with microbial ecology at a brownfield site: Interpretation, **3**, no. 4, SAB43–SAB56, doi: 10.1190/INT-2015-0057.1.

Mokni, N., and J.-D. Barnichon, 2016, Hydro-mechanical analysis of SEALEX in-situ tests — Impact of technological gaps on long term performance of repository seals: Engineering Geology, **205**, 81–92, doi: 10.1016/j.enggeo.2016.02.013.

Mokni, N., J.-D. Barnichon, P. Dick, and T. S. Nguyen, 2016, Effect of technological macro voids on the performance of compacted bentonite/sand seals for deep geological repositories: International Journal of Rock Mechanics and Mining Sciences, **88**, 87–97, doi: 10.1016/j.ijrmms.2016.07.011.

Molinero Guerra, A., N. Mokni, P. Delage, Y.-J. Cui, A. M. Tang, P. Aimedieu, F. Bernier, and M. Bornert, 2017, In-depth characterisation of a mixture composed of powder/pellets MX80 bentonite: Applied Clay Science, **135**, 538–546, doi: 10.1016/j.clay.2016.10.030.

Mudler, J., A. Hördt, D. Kreith, M. Sugand, K. Bazhin, L. Lebedeva, and T. Radic, 2022, Broadband spectral induced polarization for the detection of permafrost and an approach to ice content estimation — A case study from Yakutia, Russia: The Cryosphere, **16**, 4727–4744, doi: 10.5194/tc-16-4727-2022.

Mudler, J., A. Hördt, A. Przyklenk, A. Fiandaca, P. K. Maurya, and C. Hauck, 2019, Two-dimensional inversion of wideband spectral data from the capacitively-coupled resistivity method — First applications in periglacial environments: The Cryosphere, **13**, 2439–2456, doi: 10.5194/tc-13-2439-2019.

Müller, H. R., T. Vogt, B. Garitte, T. Sakaki, T. Spillmann, M. Hertrich, and N. Giroud, 2015, Instrumenting, monitoring and heating the full-scale emplacement (FE) experiment at the Mont Terri URL: LUCOEX Conference and Workshop: Full-Scale Demonstration Tests in Technology Development of Repositories for Disposal of Radioactive Waste.

OECD, 2003, Engineered barrier systems and the safety of deep geological repositories: State of the art report (Radioactive Waste Management).

Okay, G., P. Cosenza, A. Ghorbani, C. Camerlynck, J. Cabrera, N. Florsch, and A. Revil, 2013, Localization and characterization of cracks in clay-rocks using frequency and time-domain induced polarization: Geophysical Prospecting, **61**, 134–152, doi: 10.1111/j.1365-2478.2012.01054.x.

Okay, G., P. Leroy, A. Ghorbani, P. Cosenza, C. Camerlynck, J. Cabrera, N. Florsch, and A. Revil, 2014, Spectral induced polarization of clay-sand mixtures: Experiments and modeling: Geophysics, **79**, no. 6, E353–E375, doi: 10.1190/geo2013-0347.1.

Palmu, P. M., and E. L. Torsten, 2010, Towards an "implementing geological disposal technology platform" in Europe: 12th International Conference on Environmental Remediation and Radioactive Waste Management, 715–722.

Qiang, S., X. Shi, A. Revil, X. Kang, Y. Song, and K. Xing, 2024, Quantitative evaluation of the effect of pore fluids distribution on complex conductivity saturation exponents: Journal of Geophysical Research: Solid Earth, **129**, e2024JB028689, doi: 10.1029/2024JB028689.

Revil, A., 2000, Thermal conductivity of unconsolidated sediments with geophysical applications: Journal of Geophysical Research: Solid Earth, **105**, 16,749–16,768, doi: 10.1029/2000JB900043.

Revil, A., 2012, Spectral induced polarization of shaly sands: Influence of the electrical double layer: Water Resources Research, **48**, W02517, doi: 10.1029/2011WR011260.

Revil, A., 2013a, Effective conductivity and permittivity of unsaturated porous materials in the frequency range 1 mHz–1 GHz: Water Resources Research, **49**, 306–327, doi: 10.1029/2012WR012700.

Revil, A., 2013b, On charge accumulations in heterogeneous porous materials under the influence of an electrical field: Geophysics, **78**, no. 4, D271–D291, doi: 10.1190/GEO2012-0503.1.

Revil, A., L. M. Cathles, S. Losh, and J. A. Nunn, 1998, Electrical conductivity in shaly sands with geophysical applications: Journal of Geophysical Research: Solid Earth, **103**, 23,925–23,936, doi: 10.1029/98JB02125.

Revil, A., A. Coperey, Y. Deng, A. Cerepi, and N. Seleznev, 2018b, Complex conductivity of tight sandstones: Geophysics, **83**, no. 2, E55–E74, doi: 10.1190/geo2017-0096.1.

Revil, A., A. Coperey, D. Mao, F. Abdulsamad, A. Ghorbani, M. Rossi, and D. Gasquet, 2018a, Induced polarization response of porous media with metallic particles — Part 8. Influence of temperature and salinity: Geophysics, **83**, no. 6, E435–E456, doi: 10.1190/geo2018-0089.1.

Revil, A., A. Coperey, Z. Shao, N. Florsch, I. L. Fabricius, Y. Deng, J. R. Delsman, P. S. Pauw, M. Karaoulis, P. G. B. de Louw, E. S. van Baaren, W. Dabekaussen, A. Menkovic, and J. L. Gunnink, 2017, Complex conductivity of soils: Water Resources Research, **53**, 7121–7147, doi: 10.1002/2017WR020655.

Revil, A., and P. Cosenza 2010, Comment on "Generalized effective-medium theory of induced polarization" (Michael Zhdanov, 2008, Geophysics, 73, F197–F211): Geophysics, **75**, no. 2, X7–X9, doi: 10.1190/1.3372299.
Revil, A., J. D. Eppehimer, M. Skold, M. Karaoulis, L. Godinez, and M. Prasad, 2013, Low-frequency complex conductivity of sandy and clayey materials: Journal of Colloid and Interface Science, **398**, 193–209, doi: 10.1016/j.jcis.2013.01.015.
Revil, A., A. Ghorbani, D. Jougnot, and B. Yven, 2023a, Induced polarization of clay-rich materials — Part 1: The effect of desiccation: Geophysics, **88**, no. 4, MR195–MR210, doi: 10.1190/geo2022-0510.1.
Revil, A., A. Ghorbani, D. Jougnot, B. Yven, D. Grgic, F. Bretaudeau, and J. Deparis, 2023b, Induced polarization of clay-rich materials — Part 2: The effect of anisotropy: Geophysics, **88**, no. 6, MR305–MR322, doi: 10.1190/geo2022-0511.1.
Revil, A., A. Ghorbani, Z. Su, H. Cai, and X. Hu, 2024, Induced polarization of clay-rich materials — Part 3: Partially-saturated mixtures of clay and pyrite: Geophysics, **89**, no. 3, E101–E112, doi: 10.1190/geo2023-0562.1.
Revil, A., P. Kessouri, and C. Torres-Verdín, 2014a, Electrical conductivity, induced polarization, and permeability of the Fontainebleau sandstone: Geophysics, **79**, no. 5, D301–D318, doi: 10.1190/geo2014-0036.1.
Revil, A., Y. Qi, A. Ghorbani, M. Gresse, and D. M. Thomas, 2021, Induced polarization of volcanic rocks. 5. Imaging the temperature field of shield volcanoes: Geophysical Journal International, **225**, 1492–1509, doi: 10.1093/gji/ggab039.
Revil, A., Y. Qi, N. Panwar, M. Gresse, H. Grandis, R. Sharma, Y. Géraud, N. Chibati, and A. Ghorbani, 2022, Induced polarization images alteration in stratovolcanoes: Journal of Volcanology and Geothermal Research, **429**, 107598, doi: 10.1016/j.jvolgeores.2022.107598.
Revil, A., M. Schmutz, F. Abdulsamad, A. Balde, C. Beck, A. Ghorbani, and S. S. Hubbard 2021b, Field-scale estimation of soil properties from spectral induced polarization tomography: Geoderma, **403**, 115380, doi: 10.1016/j.geoderma.2021.115380.
Rosen, L. A., and D. A. Saville, 1991, Dielectrical spectroscopy of colloidal dispersions: Comparisons between experiment and theory: Langmuir, **7**, 36–42, doi: 10.1021/la00049a009.
Saba, S., 2013, Hydro-mechanical behaviour of bentonite-sand mixture used as sealing materials in radioactive waste disposal galleries: PhD thesis, Université Paris-Est.
Sakaki, T., B. Lüthi, T. Vogt, M. Uyama, and S. Niunoya, 2019, Heated fiber-optic cables for distributed dry density measurements of granulated bentonite mixtures: Feasibility experiments: Geomechanics for Energy and the Environment, **17**, 57–65, doi: 10.1016/j.gete.2018.09.006.
Schlumberger, C. A., 1920, Étude sur la prospection électrique du sous-sol: Gauthier-Villars, 99.
Schmutz, M., A. Revil, P. Vaudelet, M. Batzle, P. Femenía Viñao, and D. D. Werkema, 2010, Influence of oil saturation upon spectral induced polarization of oil bearing sands: Geophysical Journal International, **183**, 211–224, doi: 10.1111/j.1365-246X.2010.04751.x.
Sellin, P., and O. X. Leupin, 2013, The use of clay as an engineered barrier in radioactive-waste management a review: Clays and Clay Minerals, **61**, 477–498, doi: 10.1346/CCMN.2013.0610601.
Shirazi, S., H. Kazama, F. Salman, F. Othman, and S. Akib, 2010, Permeability and swelling characteristics of bentonite: International Journal of the Physical Sciences, **5**, 1647–1659.
Smart, N. R., A. P. Rance, and L. O. Werme, 2008, The effect of radiation on the anaerobic corrosion of steel: Journal of Nuclear Materials, **379**, 97–104, doi: 10.1016/j.jnucmat.2008.06.007.
Song, Y., X. Shi, A. Revil, and X. Kang, 2022, Monitoring in situ microbial growth and decay in soil column experiments by induced polarization: Geophysical Research Letters, **49**, e2021GL097553, doi: 10.1029/2021GL097553.
Srikanth, V., and A. K. Mishra, 2016, A laboratory study on the geotechnical characteristics of sand–bentonite mixtures and the role of particle size of sand: International Journal of Geosynthetics and Ground Engineering, **2**, 1–10, doi: 10.1007/s40891-015-0043-1.
Stern, O., 1924, Zur theorie der electrolytischen Doppelschicht (The theory of the electrolytic double layer): Zeitschrift für Elektrochemie, **30**, 508–516, doi: 10.1002/BBPC.192400182.
Tarasov, A., and K. Titov, 2007, Relaxation time distribution from time domain induced polarization measurements: Geophysical Journal International, **170**, 31–43, doi: 10.1111/j.1365-246X.2007.03376.x.
Telford, W. M., L. P Geldart, and R. E. Sheriff, 1990, Applied geophysics: Cambridge University Press.
Tong, X., L. Yan, and K. Xiang, 2023, A prediction method of compacted rock hydraulic permeability based on the MGEMTIP model: Minerals, **13**, 281–300, doi: 10.3390/min13020281.
Tournassat, C., C. I. Steefel, I. C. Bourg, and F. Bergaya, 2015, Natural and engineered clay barriers: Elsevier.
Van Voorhis, G. D., P. H. Nelson, and T. L. Drake, 1973, Complex resistivity spectra of porphyry copper mineralization: Geophysics, **38**, 49–60, doi: 10.1190/1.1440333.
Vaudelet, P., A. Revil, M. Schmutz, M. Franceschi, and P. Bégassat, 2011a, Induced polarization signature of the presence of copper in saturated sands: Water Resources Research, **47**, W02526, doi: 10.1029/2010WR009310.
Vaudelet, P., A. Revil, M. Schmutz, M. Franceschi, and P. Bégassat, 2011b, Changes in induced polarization associated with the sorption of sodium, lead, and zinc on silica sands: Journal of Colloid and Interface Science, **360**, 739–752, doi: 10.1016/j.jcis.2011.04.077.
Villar, M. V., and A. Lloret, 2008, Influence of dry density and water content on the swelling of a compacted bentonite: Applied Clay Science, **39**, 38–49, doi: 10.1016/j.clay.2007.04.007.
Vinegar, H. J., and M. H. Waxman, 1984, Induced polarization of shaly sands: Geophysics, **49**, 1267–1287, doi: 10.1190/1.1441755.
Wait, J. R., 1959, Overvoltage research and geophysical applications: Pergamon Press.
Wang, H., and A. Revil, 2020, Surface conduction model for fractal porous media: Geophysical Research Letters, **47**, e2020GL087553, doi: 10.1029/2020GL087553.
Wang, Q., A. Minh Tang, Y. J. Cui, P. Delage, J. D. Barnichon, and W. M. Ye, 2013, The effects of technological voids on the hydro-mechanical behaviour of compacted bentonite-sand mixture: Soils and Foundations, **53**, 232–245, doi: 10.1016/j.sandf.2013.02.004.
Ward, S. H., 1990, Resistivity and induced polarization methods, *in* S. H. Ward, ed., Geotechnical and environmental geophysics: SEG, SEG Series Investigations in Geophysics, 5.
Waxman, M. H., and L. J. M. Smits, 1968, Electrical conductivities in oil bearing shaly sands: SPE Journal, **8**, 107–122, doi: 10.2118/1863-A.
Wayal, V., and T. G. Sitharam, 2022, Geo-electric assessment of the compacted sand-bentonite mixes: International Journal of Geotechnical Engineering, **16**, 74–89, doi: 10.1080/19386362.2019.1692470.
Weller, A., K. Breede, L. Slater, and S. Nordsiek, 2011, Effect of changing water salinity on complex conductivity spectra of sandstones: Geophysics, **76**, no. 5, F315–F327, doi: 10.1190/geo2011-0072.1.
Weller, A., L. Slater, and S. Nordsiek, 2013, On the relationship between induced polarization and surface conductivity: Implications for petrophysical interpretation of electrical measurements: Geophysics, **78**, no. 5, D315–D325, doi: 10.1190/geo2013-0076.1.
Wieczorek, K., I. Gaus, J. C. Mayor, K. Schuster, J.-L. García-Siñeriz, and T. Sakaki, 2017, In-situ experiments on bentonite-based buffer and sealing materials at the Mont Terri rock laboratory (Switzerland): Swiss Journal of Geosciences, **110**, 253–268, doi: 10.1007/s00015-016-0247-y.
Ye, W.-M., Y.-G. Chen, B. Chen, Q. Wang, and J. Wang, 2010, Advances on the knowledge of the buffer/backfill properties of heavily-compacted GMZ bentonite: Engineering Geology, **116**, 12–20, doi: 10.1016/j.enggeo.2010.06.002.
Zhang, K., N. Chibati,, A. Revil, J. Richard, M. Gresse, Y. Xue,, and Y. Géraud, 2023, Induced polarization of volcanic rocks. 6. Relationships with other petrophysical properties: Geophysical Journal International, **234**, 2376–2394, doi: 10.1093/gji/ggad246.
Zhdanov, M. S., 2008, Generalized effective-medium theory of induced polarization: Geophysics, **73**, no. 5, F197–F211, doi: 10.1190/1.2973462.

Biographies and photographs of the authors are not available.